



저작자표시 2.0 대한민국

이용자는 아래의 조건을 따르는 경우에 한하여 자유롭게

- 이 저작물을 복제, 배포, 전송, 전시, 공연 및 방송할 수 있습니다.
- 이차적 저작물을 작성할 수 있습니다.
- 이 저작물을 영리 목적으로 이용할 수 있습니다.

다음과 같은 조건을 따라야 합니다:



저작자표시. 귀하는 원저작자를 표시하여야 합니다.

- 귀하는, 이 저작물의 재이용이나 배포의 경우, 이 저작물에 적용된 이용허락조건을 명확하게 나타내어야 합니다.
- 저작권자로부터 별도의 허가를 받으면 이러한 조건들은 적용되지 않습니다.

저작권법에 따른 이용자의 권리는 위의 내용에 의하여 영향을 받지 않습니다.

이것은 [이용허락규약\(Legal Code\)](#)을 이해하기 쉽게 요약한 것입니다.

[Disclaimer](#) 

Airway epithelial CD47 plays a critical role
in inducing influenza virus-mediated
bacterial super-infection

Sungmin Moon

Department of Medical Science
The Graduate School, Yonsei University

Airway epithelial CD47 plays a critical role
in inducing influenza virus-mediated
bacterial super-infection

Directed by Professor Ji-Hwan Ryu

The Doctoral Dissertation
submitted to the Department of Medical Science,
the Graduate School of Yonsei University
in partial fulfillment of the requirements for the degree of
Doctor of Philosophy in Medical Science

Sungmin Moon

June 2024

This certifies that the Doctoral Dissertation
of Sungmin Moon is approved.

Thesis Supervisor: Sang Sun Yoon

Thesis Committee Member#1: Ji Hwan Ryu

Thesis Committee Member#2: Jae Myun Lee

Thesis Committee Member#3: Moo Suk Park

Thesis Committee Member#4: Hyung Ju Cho

The Graduate School
Yonsei University

December 2023

ACKNOWLEDGEMENTS

I have spent several years since 2016 for the degree of doctor of philosophy. Looking back, this time will be the most precious time in my life. During this time, I realized that it is difficult to learn and understand a new field. So, I'd like to thank the Professor Ji Hwan Ryu, who gave a lot of advice and courage for me. When I first said that I wanted to do virus research, which is not done in my laboratory, he always trusted me and told that "yes, you can". I also want to say thank for Youn Wook Chung, who is my Research Associate Professor, he always took care of me and gave a lot of advice on my research. Professor Sang Sun Yoon, Professor Jae Myun Lee, Professor Moo Suk Park and Professor Hyung Ju Cho, who are my thesis committee members, gave me a lot of helpful advice and reminded me about the importance of my thesis. I also have to thank for Professor Joo-Heon Yoon, Professor Chang-Hoon Kim, Professor Min-Seok Rha, who gave me the opportunity to do a virus research. Moreover, I would also like to thank my lab colleagues and everyone around me for their support. Finally, I want to say thank for my family who always believed me and supported for me.

TABLE OF CONTENTS

ABSTRACT	vi
I. INTRODUCTION	1
II. MATERIALS AND METHODS	4
1. Cell culture	4
2. Preparation of influenza virus and bacteria	5
3. Viral-bacterial super-infection model <i>in-vitro</i>	6
4. Immunoblotting	7
5. Real-time quantitative PCR (RT-qPCR)	8
6. Flow cytometry	8
7. Short hairpin RNA (shRNA) transfection	8
8. Proteomic analysis	9
9. Bacteria adhesion/invasion assay	9
10. Measurement of paracellular permeability <i>in-vitro</i>	10
11. Measurement of transepithelial electrical resistance (TEER) <i>in-vitro</i>	11
12. Lactate Dehydrogenase (LDH) assay	11
13. Interferon (IFN) stimulation assay <i>in-vitro</i>	11
14. Immunofluorescence staining and Confocal microscopy	12
15. In-vitro pull-down assay	13
16. Mice	13
17. Viral-bacterial super-infection model <i>in-vivo</i>	14
18. Neutralizing model <i>in-vivo</i>	15
19. Bronchoalveolar lavage fluid (BALF)	15
20. Lung histologic analysis	16

21. Measurement of airway hyper-responsiveness (AHR)	16
22. Immunohistochemistry	16
23. Statistical analysis	17
III. RESULTS	18
1. Proteomic analysis of influenza virus-infected airway epithelial cells	18
2. NF- κ B/IFN signalling pathway-dependent CD47 expression in HBECs upon influenza virus infection	23
3. CD47 is upregulated and localized to the apical surface of ciliated cells following infection of HNECs and HBECs with influenza virus	28
4. Epithelial CD47 in HBECs and HNECs facilitates super-infection	33
5. Direct interactions between epithelial CD47 and the bacterial FnBP in viral- bacterial co-infected cells	42
6. Foxj1 ^{cre} -specific, but not LysM ^{cre} -specific, CD47 disruption protects mice from super-infection	49
7. Antibody-mediated CD47 neutralization protects mice from super-infection	59
8. Interaction between epithelial CD47 and bacterial FnBP is essential to cause super-infection	62
IV. DISCUSSION	67
V. CONCLUSION	71
REFERENCES	72
ABSTRACT(IN KOREAN)	80

LIST OF FIGURES

Figure 1. Proteomic analysis of influenza virus-infected airway epithelial cells.	20
Figure 2. Gene expression profiles during influenza virus infection.	22
Figure 3. Viral infection-induced CD47 expression via NF- κ B/IFN signalling pathway.	24
Figure 4. Influenza virus induces CD47 expression on the apical surface of ciliated cells in an NF- κ B-dependent manner.	25
Figure 5. Characterization of CD47 induction in the influenza virus-infected HBECs.	27
Figure 6. CD47 induction and exposure in the apical surface of ciliated HNECs following influenza virus infection.	29
Figure 7. Publicly available single-cell RNA sequencing (scRNA-seq) data of human bronchial epithelial cells.	32
Figure 8. In-vitro model of super-infection used in this study.	36
Figure 9. Protective effect of knock-down and neutralization of CD47 on super-infection in HNECs.	37
Figure 10. Knock-down and neutralization of CD47 protects HBECs from viral–bacterial co-infection.	39
Figure 11. Protective effect of knock-down and neutralization of CD47 on the <i>S. pneumoniae</i> -mediated super-infection in HBECs.	41
Figure 12. Direct interactions between epithelial CD47 and <i>S. aureus</i>	

.....45

Figure 13. Epithelial CD47 and bacterial FnBP directly interacts.47

Figure 14. Induction of CD47 upon viral infection. 51

Figure 15. Characterization of tissue-specific CD47 deletion mice. · 53

Figure 16. Two in-vivo models of super-infection used in this study.
..... 55

Figure 17. Foxj1^{Cre}-Specific, but not LysM^{Cre}-Specific, CD47
disruption protects mice from super-infection. 57

Figure 18. CD47 neutralization enhances protection against super-
infection.60

Figure 19. Interaction between epithelial CD47 and bacterial FnBP is
essential to cause super-infection. 63

Figure 20. Proposed model of viral infection-induced CD47-mediated
bacterial secondary infection. 65

LIST OF TABLES

Table 1. List of primers used in this study.	66
---------------------------------------------------	----

ABSTRACT

Airway epithelial CD47 plays a critical role in inducing influenza virus-mediated bacterial super-infection

Sungmin Moon

*Department of Medical Science
The Graduate School, Yonsei University*

(Directed by Professor Ji-Hwan Ryu)

Respiratory viral infection increases host susceptibility to secondary bacterial infections, yet the precise dynamics within airway epithelia remain elusive. Here, I elucidate the pivotal role of CD47 in the airway epithelium during bacterial super-infection. I demonstrated that upon influenza virus infection, CD47 expression was upregulated and localized on the apical surface of ciliated cells within primary human nasal or bronchial epithelial cells. This induced CD47 exposure provided attachment sites for *Staphylococcus aureus*, thereby compromising the epithelial barrier integrity. Through bacterial adhesion assays and *in vitro* pull-down assays, I identified fibronectin-binding proteins (FnBP) of *S. aureus* as a key component that binds to CD47. Furthermore, I found that ciliated cell-specific CD47 deficiency or neutralizing antibody-mediated CD47 inactivation enhanced *in vivo* survival rates. These findings suggest that interfering with the interaction between airway epithelial CD47 and pathogenic bacterial FnBP holds promise for alleviating the adverse effects of super-infection.

Key words: influenza virus, *staphylococcus aureus*, CD47, airway epithelium, bacterial super-infection, tight junction; ZO-1, fibronectin-binding protein; FnBP

Airway epithelial CD47 plays a critical role in inducing influenza virus-mediated bacterial super-infection

Sungmin Moon

*Department of Medical Science
The Graduate School, Yonsei University*

(Directed by Professor Ji-Hwan Ryu)

I. INTRODUCTION

The 1918 influenza (H1N1) pandemic claimed the lives of more than 50 million people worldwide¹. Most deaths were due to secondary bacterial pneumonia caused by common upper respiratory tract bacteria, such as *Staphylococcus aureus* and *Streptococcus pneumoniae*. Similarly, the illness of patients in the intensive care unit, infected with 2009 influenza A (H1N1), was exacerbated by secondary bacterial infections, with high morbidity and mortality rates^{2,3}. The development and extensive use of antibiotics have played a crucial role in reducing the severity of secondary bacterial infections. However, the recent emergence of antibiotic resistance has introduced a significant level of complexity to the treatment of these secondary bacterial infections⁴. Consequently, there is an urgent need to investigate and uncover the elusive molecular mechanisms responsible for secondary bacterial infections triggered by influenza.

Airway epithelial cells establish apical junctional complexes between neighboring cells to serve as a protective barrier against the external environment. Apical junctional complexes consist of apical tight junctions and underlying adherens junctions, which facilitate cell–cell adhesion and maintain barrier integrity. Zonula occludens (ZO, e.g., ZO-1) and catenin (e.g., β -catenin) proteins connect the intracellular domains of tight junctions

(e.g., Claudins and Occludin) and adherens junctions (e.g., E-cadherin) with cytoskeletal components, forming “cytosolic plaques”^{5,6}. Tight junctions play a critical role in regulating the passage of ions and solutes through the paracellular space, effectively blocking the translocation of pathogens from the lumen to the interstitium. Consequently, viral infections that disrupt tight junctions can facilitate the translocation of pathogens and receptor exposure⁷⁻¹⁰. Thus, preserving the integrity of this barrier is crucial in preventing bacterial infection.

Respiratory viral infection increases host susceptibility to bacterial pathogens by *i*) interfering with antibacterial innate immune responses via interferon (IFN) induction¹¹⁻¹⁷ and depletion of alveolar macrophages¹⁸; or *ii*) providing binding sites for bacteria, including cellular receptors, such as intercellular adhesion molecule-1 (ICAM-1)¹⁹⁻²³, carcinogenic embryonic adhesion molecule 1 (CEACAM1)^{20,24}, platelet-activating factor receptor (PAF-r)^{20,24}, or extracellular matrix (ECM) proteins, such as fibronectin (FN)^{24,25}. Given that PAF-r binds to the phosphorylcholine on *S. pneumoniae*'s cell wall, it has been proposed as a potential therapeutic target for secondary bacterial infections^{26,27}. However, the use of a PAF-r antagonist did not demonstrate any effect in the secondary bacterial infection model²⁸. As a result, it is essential to explore intervention strategies that specifically focus on disrupting the interaction between bacteria and cell receptors, utilizing antibody-mediated blockade, in treatment approaches.

CD47, also known as integrin-associated protein (IAP), is a widely expressed transmembrane glycoprotein. It serves as a “don't-eat-me” signal by interacting with the inhibitory receptor signal-regulatory protein alpha (SIRP α) on myeloid immune cells, thereby inhibiting phagocytosis of CD47-expressing erythrocyte²⁹. Cancer and viral-infected hematopoietic cells overexpress CD47 for immune evasion^{30,31}. Meanwhile, in non-hematopoietic cells, CD47 plays a role in tissue repair, contributing to improved healing and survival in various models such as skin thermal injury³², organ transplant³³⁻³⁷, and intestinal mucosal injury³⁸. Notably, the specific involvement of CD47 in airway epithelium during super-infection remains unexplored. In a proteomics analysis of nasal

epithelial cells infected with influenza virus, I observed the presence of CD47. Through the validation process, I uncovered that CD47 induced by viral infection was not only detected in the colonization site (nasal epithelium) but also at the site of infection (bronchial epithelium). Given that CD47 seems to be predominantly expressed in FoxJ1⁺ cells (deuterosomal cells and, to a lesser extent, multi-ciliated cells) based on single-cell RNA sequencing and immunostaining analysis of upper and lower airway primary epithelial cells, I initiated an investigation into the involvement of CD47 in secondary bacterial infections using a FoxJ1⁺ cell-specific CD47 gene-deletion mouse model and CD47 neutralizing antibodies. In my pursuit to identify a bacterial component that interact with CD47, I conducted experiments involving five *S. aureus* mutant strains with deleted cell wall-anchored proteins. Remarkably, my investigations revealed that only fibronectin-binding proteins (FnBP) exhibited a strong affinity for CD47. To further solidify my findings, I employed a combination of FoxJ1⁺ cell-specific CD47 gene-deletion mice and a FnBP mutant strain of *S. aureus* in the context of super-infection. This approach allowed us to establish that the specific interaction between airway epithelial CD47 and bacterial FnBP plays a pivotal role in causing super-infection. By comprehensively exploring the role of CD47 in facilitating secondary bacterial infections, this study may pave the way for the development of innovative therapeutic approaches, ultimately leading to improved clinical outcomes for patients.

II. MATERIALS AND METHODS

1. Cell culture

All experiments using human nasal epithelial cells (HNECs) were approved by the institutional review board of Yonsei University College of Medicine (4-2016-1153 and 4-2021-0573). Passage #2 HNECs were seeded at a density of 1×10^5 cells on a 12-mm, 0.45- μ m pore Transwell-clear culture insert (Corning, Tewksbury, MA, USA) and incubated at 37 °C in a humidified 5% CO₂ incubator. The cells were cultured in a 1:1 mixture of bronchial epithelial cell growth media and DMEM, supplemented with growth factors according to the manufacturer's instructions (Lonza, Basel, Switzerland). After reaching confluence under submerged culture conditions, the cells were maintained in an air-liquid interface (ALI) culture system by removing the medium from the apical chamber. Culture medium was changed every other day for 14 days. Human bronchial epithelial cells (HBECs) were cultured according to the manufacturer's instructions (Lonza, Basel, Switzerland). HBECs used in this study were obtained from four non-asthmatic adult donors: a 43-year-old male (Hispanic), a 52-year-old male (Hispanic), a 66-year-old male (Hispanic), and a 48-year-old female (Caucasian). Briefly, the cells were seeded and expanded in T-75 flasks using bronchial epithelial growth media (Lonza, Basel, Switzerland) containing the recommended supplements BEGM™ SingleQuots™ Kit (Lonza, Basel, Switzerland) at 37 °C and 5% CO₂ in a humidified incubator. After 80% confluence was reached, the cells were detached using ReagentPack™ (Lonza, Basel, Switzerland) and seeded at a density of 5×10^4 cells on rat tail collagen (Corning, Bedford, MA, USA)-coated Transwell inserts (6.5 mm, 0.4 μ m pore; Corning, Tewksbury, MA, USA). The cells were cultured using BEGM in both apical and basolateral compartments until the cells became confluent (approximately 3 days). Once confluent, the cells were placed under air-liquid interface (ALI) culture conditions; the apical compartments were exposed to air, and the basolateral compartments were supported by bronchial ALI (B-ALI) differentiation media containing the recommended supplements BEGM™ SingleQuots™

Kit. The B-ALI differentiation media were changed on alternative days for 21 days. Madin-Darby canine kidney (MDCK) cells were obtained from American Type Culture Collection (ATCC, Manassas, Virginia, USA). MDCK cells were incubated in 37 °C and 5% CO₂ in a humidified incubator using Eagle's minimum essential medium (ATCC, Manassas, Virginia, USA) supplemented with 10% fetal bovine serum (FBS) (Thermofisher, Waltham, MA, USA) and 1% penicillin–streptomycin (Thermofisher, Waltham, MA, USA). The passage number for all MDCK cells used in this study was less than 50. A549 cells were obtained from American Type Culture Collection (ATCC, Manassas, Virginia, USA) and grown at 37 °C and 5% CO₂ in a humidified incubator using Dulbecco's modified Eagle medium (DMEM) (Lonza, Basel, Switzerland) supplemented with 10% FBS and 1% penicillin–streptomycin. For all influenza virus infections, the medium used in this study was DMEM supplemented with 5% FBS and 1% penicillin–streptomycin. For superinfection, DMEM supplemented with 5% FBS without antibiotics was used. In the *NF-κB* pathway inhibition experiment, HBECs were treated with dimethyl sulfoxide (DMSO) or 10 μM of caffeic acid phenethyl ester (Sigma-Aldrich, St. Louis, MO, USA) for 1 h before viral infection.

2. Preparation of influenza virus and bacteria

Influenza A virus /Korea/01/2009 (pH1N1) was provided by Man-Seong Park's laboratory (Korea University, Seoul, Republic of Korea). *Staphylococcus aureus* (*S. aureus*) (American Type Culture Collection, Manassas, VA) and *Streptococcus pneumoniae* (*S. pneumoniae*) (National Culture Collection for Pathogens, Cheongwon, Korea), GFP-tagged *S. aureus* were obtained from Sang Sun Yoon's laboratory (Yonsei University, Seoul, Republic of Korea). Influenza A virus /Korea/01/2009 (pH1N1) used in this study was propagated in embryonated chicken eggs as previously described⁶⁵. Viruses were harvested via centrifugation of allantoic fluid or culture medium at 1,300 × *g* for 10 min. They were stored at -80 °C, and viral titers were determined in a plaque assay⁶⁵. Briefly, MDCK cells in a monolayer were inoculated with serially diluted viral stocks for 1 h. After adsorption for 1 h, the unbound viral particles were removed, and the cells were overlaid with

Minimum Essential Medium (MEM) containing 1% agarose and 1 $\mu\text{g}/\text{mL}$ of tosyl phenylalanyl chloromethyl ketone (TPCK)-treated trypsin (Sigma-Aldrich, St. Louis, MO, USA). After incubation for 72 h, the cells were stained with 1% crystal violet, and viral titers were determined by counting the plaques. *S. aureus* (ATCC, Manassas, Virginia, USA) and *S. pneumoniae* (NCCP, Cheongwon, Korea) were cultured on a Bacto™ brain heart infusion (BHI; BD Biosciences, San Jose, CA, USA) agar plate at 37 °C⁶⁶. For the culture of GFP-tagged *S. aureus* strain, 2.5 mg/mL of tetracycline-hydrochloride (Sigma-Aldrich, St. Louis, MO, USA) was added. *S. aureus* laboratory strains 8325-4 (FnBP A+/B+) and DU5883 (FnBP A-/B-) were cultured on BHI agar plate, other strains DU5883 (pFNBA4; FnBP A+/B-), DU5883 (pFNBA4; A-/B+) were cultured on BHI agar plates with chloramphenicol at 10 $\mu\text{g}/\text{ml}$ at 37 °C, respectively. *P. aeruginosa* and *S. epidermidis* were cultured on Luria-Bertani (LB) agar plates and Tryptic Soy Agar (TSA) plates at 37 °C, respectively.

For *in vitro* pull-down assay, five *S. aureus* mutant strains of cell wall-anchored proteins (CWAs), namely JE2 *fnbB::Tn* (NE728), JE2 *sasG::Tn* (NE825), JE2 *isdB::Tn* (NE1102), JE2 *sdrE::Tn* (NE98), and JE2 *clfA::Tn* (NE543), all of which were obtained from the Nebraska Transposon Mutant Library (BEI resources, Manassas, VA, USA)⁶⁷. The absence of CWAs in these mutants was validated through PCR using specific primers. The wild-type (WT) control used for this study was the Methicillin-resistant *S. aureus* (MRSA) strain USA300 JE2. The WT JE2 strain was cultured at 37°C on TSA plates, while the other mutant strains were cultured at 37 °C on TSA plates supplemented with 10 $\mu\text{g}/\text{mL}$ erythromycin.

3. Viral-bacterial super-infection model *in-vitro*

For *in vitro* super-infection experiments, fully differentiated HNECs or HBECs were infected with phosphate-buffered saline (PBS) or influenza virus at a multiplicity of infection (MOI) 1 and incubated for 2 h. After viral infection, cells were washed twice with PBS and supplied with fresh media. The following day, the virus-infected cells were

infected with PBS or *S. aureus* at MOI 5 (HNECs) or at MOI 3 (HBECs) or *S. pneumoniae* at MOI 5 (HBECs), and incubated for 3 h. After bacterial infection, cells were washed twice with PBS and supplied with fresh media supplemented without gentamycin.

4. Immunoblotting

Primary epithelial cells and mouse lung tissues were lysed in RIPA buffer (Sigma-Aldrich, St. Louis, MO, USA) with Halt™ Protease & Phosphatase Inhibitor Single-Use Cocktail, EDTA-free (100x) (Thermo Fisher Scientific, Inc, Waltham, MA, USA). Equal concentrations of proteins (25 µg) were separated using 8–12% SDS-PAGE gels and transferred to PVDF membranes (Merck Millipore, Darmstadt, Germany). After blocking with 5% skim-milk or bovine serum albumin (BSA) in Tris-buffered saline (50 mM Tris-Cl, pH 7.5, 150 mM NaCl) containing 0.5% Tween 20 (TTBS) for 1 h at RT, the membranes were incubated with primary antibodies (1:1,000) in 5% skim-milk or BSA with TTBS at 4 °C overnight. The membranes were then washed three times with TTBS and incubated with secondary antibodies diluted (1:1,000) in 5% skim-milk or BSA with TTBS for 1 h. Blots were visualized using Pierce ECL Western Blotting Substrate (Thermo Fisher Scientific, Inc, Waltham, MA, USA) and exposed to X-ray film. Primary antibodies used in immunoblotting as follows: rabbit anti-ZO-1 antibody (Thermo Fisher Scientific, Inc, Waltham, MA, USA), mouse anti-ZO-1 (Thermo Fisher Scientific, Inc, Waltham, MA, USA), mouse anti-CD47 antibody (Thermo Fisher Scientific, Inc, Waltham, MA, USA), mouse anti-ICAM-1 (Santa Cruz, Dallas, Texas, USA), rabbit anti-p65 (Cell Signaling technology, Danvers, MA, USA), rabbit anti-phospho-p65 (Ser536) (Cell Signaling technology, Danvers, MA, USA), mouse monoclonal anti-CD47 (R&D systems, Minneapolis, MN, USA), mouse anti-β-actin (Santa Cruz, Dallas, Texas, USA), and mouse anti-GAPDH (Santa Cruz, Dallas, Texas, USA). Secondary antibodies used as follows: Peroxidase AffiniPure goat anti-rabbit IgG (H+L) (Jackson ImmunoResearch, West Grove, Pennsylvania, USA), mouse anti-goat IgG-HRP (Santa Cruz, Dallas, Texas, USA), and goat anti-mouse IgG (H+L)-HRP (GenDEPOT, Barker, Texas, USA).

5. Real-time quantitative PCR (RT-qPCR)

Total RNA was isolated from HNECs, HBECs, and mouse lung tissues using Hybrid-R™ (GeneAll, Seoul, Republic of Korea). cDNA was synthesized via reverse-transcription using 500 ng of RNA with random hexamer primers (*Invitrogen*, Carlsbad, CA, USA), RNase inhibitor (*Applied Biosystems*, Foster City, CA, USA), dNTPs (*Applied Biosystems*, Foster City, CA, USA), and M-MLV reverse transcriptase (*Invitrogen*, Carlsbad, CA, USA). For real-time qPCR, KAPA SYBR FAST qPCR master mix (2X) was used according to the manufacturer's instruction. PCR reaction was performed using QuantStudio 3 Real-Time PCR System (*Applied Biosystems*, Foster City, CA, USA). The gene expression levels were evaluated using the comparative Ct method ($2^{-\Delta\Delta C_t}$ method). Primers used for real-time qPCR in this study are listed in Table 1.

6. Flow cytometry

Cells were detached from culture plates and separated using a mixture of non-enzymatic cell dissociation solution (*Sigma-Aldrich*, St. Louis, MO, USA) and trypsin-EDTA in a 1:1 ratio. Cells were incubated with 1 μ g of mouse IgG isotype control antibody (*Thermo Fisher Scientific, Inc*, Waltham, MA, USA) or mouse anti-hCD47 APC-conjugated antibody (*Abcam*, Waltham, MA, USA) for 20 min on ice. Cells were analyzed using the BD FACSLyric™ (*BD Biosciences*, San Jose, CA, USA). Nonviable cells were excluded from further analyses. Data were acquired with BD FACSuite v1.3 (*BD Biosciences*, San Jose, CA, USA) and analyzed with FlowJo™ v10.6.2 software (*BD Biosciences*, San Jose, CA, USA).

7. Short hairpin RNA (shRNA) transfection

For the knock-down of human *CD47*, a plasmid-based lentiviral shRNA was purchased from Lugen Sci. The sequence for the *CD47*-specific shRNA was 5'-GCA TGG CCC TCT TCT GAT TTC-3', and that for scrambled shRNA (sc-shRNA) was 5'-GCA CTA CCA GAG CTA ACT CAG ATA GTA CT-3'. HNECs or HBECs (passage #2) were transfected with

lentiviral shRNAs (MOI 10) using polybrene reagent (Lugen Sci Co., Ltd, Seoul, Republic of Korea). After a 24-h incubation, cells were supplied with fresh media. Once confluent, the cells were placed under ALI culture conditions; the apical compartments were exposed to air, and the medium for basolateral compartments was changed every other day for 14 days (HNECs) or 21 days (HBECs).

8. Proteomic analysis

Isobaric tag for relative and absolute quantification (iTRAQ) or Tandem Mass Tag (TMT) proteomic methods were used to identify total protein expression differences between uninfected or influenza virus-infected HNECs. Cells were lysed in RIPA buffer (Sigma-Aldrich, St. Louis, MO, USA) with Halt™ Protease & Phosphatase Inhibitor Single-Use Cocktail, EDTA-free (100x) mixture (Thermo Fisher Scientific, Inc, Waltham, MA, USA). Acetone-precipitated protein pellets were stored at -80 °C. Proteins from HNECs or HBECs were labeled using the 8plex iTRAQ labeling kit (SCIEX, Warrington, UK) or the TMT 10plex isobaric label reagent set (Thermo Fisher Scientific, Inc, Waltham, MA, USA), respectively, according to the manufacturer's instructions. The labeled peptides were pooled and then dried using SpeedVac (Thermo Fisher Scientific, Inc, Waltham, MA, USA). Strong cation exchange fractionation, liquid chromatography (LC)-mass spectrometry (MS), database searching, and quantitative data analysis were performed by Poochon Scientific (Frederick, MD, USA) as previously described⁶⁸. The mass spectrometry proteomics data have been deposited to the ProteomeXchange Consortium via the PRIDE partner repository with the data set identifier PXD042618. Proteomics data analysis was performed using the Database for Annotation, Visualization and Integrated Discovery (DAVID) v6.8 (<https://david.ncifcrf.gov/tools.jsp>).

9. Bacteria adhesion/invasion assay

HBECs and A549 cells were infected with PBS or influenza virus at MOI 1. After incubation for 2 h, cells were washed twice with PBS and supplied with fresh media. The

following day, the virus-infected cells were subjected to PBS or infected with *S. aureus* at MOI 10 (A549) or *S. aureus* laboratory strain 8325-4 (FnBP A+/B+) and three mutant strains (FnBP A+/B-, A-/B+, and A-/B-) at MOI 3 (HBECs). After incubation for 3 h, cells were washed twice with PBS to remove unbound bacteria and lysed with 0.8 mL of 0.025% Triton X-100. After serial dilutions with PBS, the number of bacteria bound to the cells was quantified⁶¹. For CD47 neutralization, virus-infected cells were treated with 5 µg/mL of IgG1 control antibodies (Invitrogen, Carlsbad, CA, USA) or 5 µg/mL of α-hCD47 neutralizing antibodies (Invitrogen, Carlsbad, CA, USA) for 2 h, followed by bacteria infection for 3 h. For *in vivo* bacterial adhesion assay, the infected mice were euthanized, and the lung was collected. The lung tissue was homogenized in PBS and centrifuged at 500 × g for 5 min. Following centrifugation, the supernatant was discarded, and the sediments were re-suspended with 0.025% Triton X-100. Subsequently, after serial dilutions with PBS, the number of bacteria bound to the cells was quantified⁶¹. For *in vivo* bacterial invasion assay, the lung tissue was incubated with PBS containing 1% penicillin-streptomycin at 37 °C with 5% CO₂ for 1 h to remove extracellular and surface-adherent bacteria. After the incubation period, the lung tissue was homogenized and centrifuged, and then the sediments were re-suspended with 0.025% Triton X-100. Following serial dilutions with PBS, the number of bacteria bound to the cells was quantified⁶¹.

10. Measurement of paracellular permeability *in-vitro*

After infection or treatment, transwell inserts were transferred to new cell culture plates (Corning, Tewksbury, MA, USA). After two PBS washes, the apical compartments of transwell were treated with 4 kDa FITC-dextran (Sigma-Aldrich, St. Louis, MO, USA), and basolateral compartments of transwell were replaced with Hank's Balanced Salt Solution (WELGENE, Gyeongsan-si, Korea). After incubation for 2 h, basolateral compartments were collected and analyzed using BioTek Cytation™ 5 Cell Imaging Multi-Mode Reader (BioTek Instruments, Winooski, VT, USA).

11. Measurement of transepithelial electrical resistance (TEER) *in-vitro*

The electric resistance of the respiratory epithelium was determined by measuring TEER in HNECs or HBECs using the EVOM[®] resistance meter and Endohm[®] chamber (World Precision Instruments, Sarasota, Florida, USA). The values for cell-covered transwell inserts were expressed in standard units of ohms per square centimeter (Ω/cm^2) after subtracting the resistance of blank transwell inserts and presented as mean \pm standard error of mean (SEM).

12. Lactate Dehydrogenase (LDH) assay

Following viral, bacterial and/or super-infection, cell cytotoxicity was measured using CytoTox 96 Non-Radioactive Cytotoxicity Assay kit (PROMEGA, Madison, WI, USA) according to the manufacturer's instructions. Briefly, apical and basolateral supernatants of HNECs and HBECs were collected and incubated with the reagent for 30 min in a 96-well plate. Results were obtained at 490 nm using a spectrophotometer. Positive control was supplied with the kit, while PBS or culture medium was used as the negative control. Data was analyzed with SoftMax Pro Software v5.2 (Molecular Devices, Sunnyvale, CA, USA).

13. Interferon (IFN) stimulation assay *in-vitro*

For type I and III interferon (IFN) stimulations, basolateral region of hBECs were treated with recombinant human (rh) IFN- β protein (R&D systems, Minneapolis, MN, USA) using 0.1, 1, 10, 100, 1000 U/mL and recombinant human (rh) IL-29/IFN- λ 1 protein (R&D systems, Minneapolis, MN, USA) using 0.1, 1, 10, 100 ng/mL for 24 h, respectively. To validate IFN stimulation, the induction of interferon-stimulated genes (ISGs) were analyzed by qPCR. To block type I IFN signaling experiment, 2 $\mu\text{g}/\text{mL}$ of IFNAR1 (Abcam, Waltham, MA, USA) and normal goat IgG control antibody (R&D systems, Minneapolis, MN, USA) were treated with basolateral region for 1 h prior to the rhIFN- β protein treatment. Similarly, to block type III IFN signaling experiment, 10 $\mu\text{g}/\text{mL}$ of IFN λ R1 (PBL assay science, NJ, USA), mouse IgG isotype control antibody (Invitrogen, Carlsbad, CA,

USA) were treated with basolateral region for 1 h prior to the rhIFN- λ 1 protein treatment.

14. Immunofluorescence staining and Confocal microscopy

For immunofluorescence (IF) staining, cell slides were fixed with 4% paraformaldehyde (PFA) for 20 min, permeabilized with 0.1% Triton X-100 (Amresco, Solon, OH, USA) in PBS for 5 min, and treated with 50 mM NH₄Cl (Sigma-Aldrich, St. Louis, MO, USA) in PBS for 15 min. After incubation in a blocking solution containing 0.1% bovine serum albumin (BSA), 0.1% Triton X-100, 1% normal donkey serum (NDS) for 1 h at room temperature (RT), the slides were incubated with primary antibodies diluted in Dako antibody diluent (Dako, Santa Clara, CA, USA) at 4 °C overnight and with secondary antibodies in diluted in Dako antibody diluent at RT for 1 h. For mouse trachea IF staining, trachea was fixed in 4% PFA for 24 h. Trachea samples were transferred to 50% OCT compound in PBS for 24 h, sequentially transferred to 100% OCT compound for 24 h, embedded in Tissue-Tek OCT compound (Sakura Finetek, CA, USA), snap-frozen in liquid nitrogen, and stored at -80 °C. All sections were cut at 8 μ m in a cryostat microtome. Cryosections on slides were covered with 3% peroxidase blocking solution (Dako, Santa Clara, CA, USA) for 10 min at RT. After the inactivation of endogenous peroxidase, slides were washed twice with 1% TBS. Blocking was conducted using 5% BSA at RT for 1 h. The slides were incubated with primary antibodies (1:100) diluted in Dako antibody diluent at 4 °C overnight. The following day, slides were washed three times with 1% TBS and then incubated with secondary antibodies diluted with Dako antibody diluent at RT for 1 h. After final washing, the slides were cover-slipped with Fluoroshield™ and DAPI (Sigma-Aldrich, St. Louis, MO, USA). Confocal images were acquired by a confocal laser-scanning microscopy (LSM980, Carl Zeiss MicroImaging GmbH, Jena, Germany) and analyzed by ZEN image software (ZEN 3.0 lite, Carl Zeiss MicroImaging GmbH, Jena, Germany). Cytospin experiments were conducted as previously described⁶⁴. Primary antibodies used in IF staining as follows: rabbit anti-ZO-1 (Thermo Fisher Scientific, Inc, Waltham, MA, USA), mouse anti-hCD47 (Thermo Fisher Scientific, Inc, Waltham, MA, USA), goat anti-

mCD47 (R&D systems, Minneapolis, MN, USA), rabbit anti- α -tubulin (Abcam, Waltham, MA, USA), rabbit anti-MUC5AC (Cell Signaling technology, Danvers, MA, USA), rabbit polyclonal anti-Influenza A NP (Thermo Fisher Scientific, Inc, Waltham, MA, USA), mouse monoclonal anti-p63 (Santa Cruz, Dallas, Texas, USA), and rabbit anti-*S. aureus* (Abcam, Waltham, MA, USA). Secondary antibodies used in IF staining as follows: Alexa Fluor 488 donkey anti-mouse IgG (Molecular Probes, Eugene, Oregon, USA), Alexa 488 donkey anti-rabbit IgG (Molecular Probes, Eugene, Oregon, USA), Alexa Fluor 568 goat anti-mouse IgG (Molecular Probes, Eugene, Oregon, USA), Alexa Fluor 568 goat anti-rabbit IgG (Molecular Probes, Eugene, Oregon, USA), and Alexa Fluor 647 donkey anti-goat IgG (Molecular Probes, Eugene, Oregon, USA).

15. In-vitro pull-down assay

His-tagged human CD47 protein (250 ng) (Acro biosystems, Newark, Delaware, USA) and 1×10^2 colony-forming units (CFUs) of bacteria were mixed, and the mixtures were isolated using Dynabeads™ His-Tag Isolation & Pulldown kit (Invitrogen, Carlsbad, CA, USA) according to the manufacturer's instructions. After placing the tube on DynaMag™-2 magnet (Invitrogen, Carlsbad, CA, USA), the beads were washed twice with 1 x binding/wash buffer, and the supernatant was removed. The washed buffers (*supernatants*) and the final beads (*pellets*) were plated on a BHI agar plate and TSA plate containing 10 μ g/mL erythromycin, separated using 12% SDS-PAGE gel, and blotted with anti-human CD47 antibody (Thermo Fisher Scientific, Inc, Waltham, MA, USA).

16. Mice

C57BL/6J background *CD47* floxed (*Cd47^{fl/fl}*) mice were purchased from the Mouse Biology Program at UC Davis, CA, USA (*Cd47^{tm1c(KOMP)Mbp/Mmucd}*, 046999-UCD). *Rosa26-tdTomato* reporter mice were kindly provided by Dr. Jinwoong Bok (Yonsei University College of Medicine, Seoul, Republic of Korea). *Foxj1^{Cre}* transgenic and *LysM^{Cre}* knock-in/knock-out mice were kindly provided by Dr. Michael J. Holtzman

(Washington University School of Medicine, St. Louis, MO, USA) and Dr. Hyoung-Pyo Kim (Yonsei University College of Medicine, Seoul, Republic of Korea), respectively. *Foxj1^{Cre};Cd47^{fl/fl}* (*Cd47^{Foxj1}*), *LysM^{Cre};Cd47^{fl/fl}* (*Cd47^{LysM}*), and *Cd47^{fl/fl}* mice were bred in-house at Yonsei University College of Medicine in Seoul, Republic of Korea. Mice were used at 6–8 weeks of age and housed in the specific pathogen-free (SPF) animal facilities under a 12 h light-dark cycle at 20 ± 2 °C, a humidity of $50 \pm 5\%$, ventilation of 10-15/h, the light of 150-300 Lux, noise of less than 60 dB and maintained on normal chow diet. All experiments involving animals were conducted following the guidelines for the Care and Use of Laboratory Animals and approved by the Institutional Animal Care and Use Committee at Yonsei University College of Medicine (protocol number 2022-0257), according to guidelines outlined by the Association for Assessment and Accreditation of Laboratory Animal Care (AAALAC) International (facility number 001071). The genotypes of mice were determined using PCR amplification of tail DNA using primers listed in Table 1.

17. Viral-bacterial super-infection model *in-vivo*

Six to seven-week-old mice (18–21 g body weight) were used. Mice were anesthetized by intraperitoneal injection (i.p.) of Zoletil: Rompun: PBS (1:1:8) mixture (100 μ L) and infected intranasally with PBS or 100 plaque-forming units (PFUs) of influenza virus (30 μ L) at day 0. For the super-infection model, uninfected or virus-infected mice were infected intranasally with PBS or 1×10^8 CFU of *S. aureus* (20 μ L) at day 7. Following viral infection, mice were monitored daily for changes in weight and mortality until day 29. Mice manifesting a weight loss exceeding 30% of their initial body weight were humanely euthanized and subsequently excluded from further analysis in both weight loss and survival data, in accordance with the humane euthanasia criteria defined by the relevant animal protocols. Weight loss (or discovery of mice found dead) was the sole criterion for determining mortality in my study. Clinical scores were not used as an additional parameter for declaring a mouse dead.

18. Neutralizing model *in-vivo*

C57BL/6 mice were purchased from Orient Bio INC. (Suwon, Republic of Korea) and six to seven-week-old male mice (18-21 g body weight) were used. Mice were anesthetized and infected intranasally with 10 PFU of influenza virus at day 0. On days 5 and 7 after viral infection, mice were injected intranasally with either IgG2a control antibodies (clone 2A3; Cat.BE0089; BioXcell, West Lebanon, NH, USA) or anti-mouse CD47 antibodies (clone MIAP301; Cat.BE0270; BioXcell, West Lebanon, NH, USA). On day 7, 30 min after the second treatment of antibodies, mice were infected intranasally with 5×10^5 CFU of *S. aureus*.

19. Bronchoalveolar lavage fluid (BALF)

After whole-body perfusion, the mouse right lung lobe and the spleen were used for quantification of bacterial CFU, and left lobe was used for H&E staining for counting inflammatory cells. BAL fluids were collected from the lungs after washing with ice-cold PBS (1 mL). After centrifugation at $1,700 \times g$ for 5 min, the supernatants were collected and stored at -80°C . The pellets of BAL fluid were resuspended with 1 mL of 2% FBS in PBS and then counted using EVE™ automated cell counter (NanoEnTek, Seoul, Republic of Korea). Total protein concentration in mouse BAL fluid was measured using Pierce™ BCA protein assay kit according to the manufacturer's instructions (Thermo Fisher Scientific, Inc, Waltham, MA, USA). Albumin in mouse BAL fluid was quantified using the BCG albumin assay kit (Sigma-Aldrich, St. Louis, MO, USA) according to the manufacturer's instructions. Levels of IL-6 (DY406) and TNF- α (DY410) in mouse BAL fluid were quantified using DuoSet® ELISA kit (R&D Systems, Minneapolis, MN, USA), according to the manufacturer's instructions. The ELISA detection limits for IL-6 and TNF- α were consistently greater than pg/mL. The sample absorbance was measured at 450 nm using a VersaMax™ Microplate Reader (Molecular Devices, Sunnyvale, CA, USA). Data was analyzed with SoftMax® Pro Software v5.2 (Molecular Devices, Sunnyvale, CA, USA).

20. Lung histologic analysis

Lung tissues were fixed in 4% PFA for 24 h and embedded in paraffin. The mouse lung tissues were sectioned and stained with hematoxylin and eosin (H&E) to count inflammatory cells that infiltrated the lungs. Lung injury was scored as previously described⁷¹. Briefly, blinded adults were scored using lung sections stained with H&E. The severity of inflammation and pneumonia was evaluated based on the number of perivascular lymphocytic infiltration, peribronchial lymphocytic infiltration, bronchitis, and alveolar hemorrhage using the following scoring system: 0, absence; 1, mild; 2, moderate; and 3, severe.

21. Measurement of airway hyper-responsiveness (AHR)

Airway hyper-responsiveness (AHR) was measured as the change in airway function using whole-body plethysmography (Buxco Electronics Ltd., Wilmington, USA) as previously described⁷⁰. Briefly, mice were placed unrestrained in a chamber connecting a transducer to measure pressure changes inside the chamber. After acclimation, increasing concentrations of methacholine (0, 6.25, 12.5, 25, and 50 mg/mL) were nebulized for 3 min, and enhanced pause (Penh, a dimensionless unit, correlates with pulmonary resistance) was measured for 2 min using FinePoint software (Buxco Electronics Ltd., Wilmington, USA).

22. Immunohistochemistry

Formalin-fixed paraffin sections (4 μ m) from mouse trachea and lung were de-waxed in xylene (Sigma chemicals, St. Louis, MO, USA), and then rehydrated in ethanol. Antigen retrieval was performed using 0.01 mol/L sodium citrate buffer (pH 6.0). Quenching endogenous peroxidase activity was covered with 3% peroxidase blocking solution (Dako, Santa Clara, CA, USA) for 10min at room temperature (RT). Blocking step was performed with 10% normal serum from VECTASTAIN Elite ABC Kit (Vector Laboratories, Burlingame, CA, USA). For 3, 3'-diaminobenzidine tetrahydrochloride (DAB) staining of mouse CD47 in mouse trachea and lung, mouse CD47 (R&D systems, Minneapolis, MN,

USA) antibody was applied (1:1000) for overnight at 4°C. DAB Staining was visualized using Olympus BX43 microscope with Olympus cellSens Entry software (Hamburg, Germany).

23. Statistical analysis

Data are analyzed by GraphPad Prism v10.1.0 software and expressed as mean \pm SEM. A Student's t-test was employed for single-variable comparisons, one-way ANOVA was utilized for multiple comparisons, and two-way ANOVA was applied for analyses involving multiple variables. Values of p less than 0.05 were considered statistically significant.

III. RESULTS

1. Proteomic analysis of influenza virus-infected airway epithelial cells

Limited research has investigated the local surface remodeling of primary human nasal epithelial cells (HNECs) in the context of viral infection^{10,23,24,39}. Consequently, the complete spectrum of upregulated adhesion molecules during respiratory viral infections that facilitate bacterial attachment and invasion remains unknown. To address this gap, the current study provides a comprehensive view of HNEC responses to influenza virus pH1N1 infection, via global proteome profiling of uninfected (Mock, $n = 4$) and influenza-infected (Virus-only, $n = 4$) HNECs with isobaric tags using relative and absolute quantitation (iTRAQ) technique. A total of 3583 proteins were detected, 89 of which were significantly increased (52 proteins) or decreased (37 proteins) in the virus-infected HNECs compared to mock-infected controls ($p < 0.05$) (Figure 1A). Kyoto Encyclopedia of Genes and Genomes (KEGG) pathway analysis revealed four significantly enriched virus-related pathways in the virus-infected HNEC proteome, including “Influenza A” (Figure 1C). At three days post-infection (dpi), viral gene expression was elevated, accompanied by an increase in host innate immune responses, particularly type-I and type-III interferons (IFNs) (Figure 2A and 2B), while type-II IFN remained unchanged. Following viral infection, two candidate proteins displayed increased peptide expression and were expected to localize in the cellular membrane: leukocyte surface antigen CD47 (Q08722, FC = 1.15, $p = 0.001$), and carcinoembryonic antigen-related cell adhesion molecule 5 (CEACAM5, P06731, FC = 1.14, $p = 0.028$) (Figure 1B). Among these candidates, CD47 was selected for further investigation, and its expression was validated in HNECs (Figure 6) and primary human bronchial epithelial cells (HBECs) (Figure 4). Subsequent to viral infection, ZO-1 abundance decreased, and its cellular connections were disrupted, while CD47 exhibited increased expression in both HNECs (Figure 6A-C) and HBECs (Figure 4A-C). In line with a prior study³⁸, functional annotation using gene ontology (GO) analysis demonstrated that CD47’s biological processes were linked to *response to stimulus-related* GOs, *cell*

migration-related GOs, *immune system process-related* GOs, cell surface receptor signaling pathway, and cellular component organization (Figure 1D).

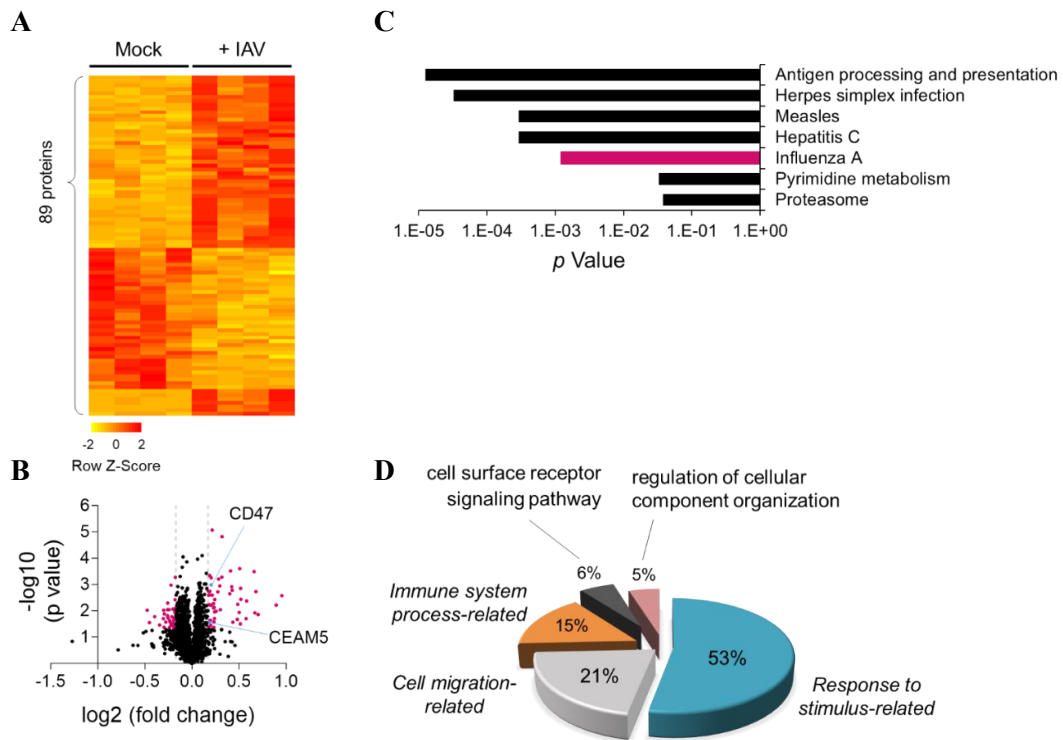


Figure 1. Proteomic analysis of influenza virus-infected airway epithelial cells. Proteomic characterization of human nasal epithelial cells (HNECs), uninfected (*mock*, $n = 4$) or infected with influenza virus (+ *influenza virus*, $n = 4$), using Isobaric tags for relative and absolute quantitation (iTRAQ). Cell lysates were harvested on day 5 post-infection (dpi). A total of 3,583 proteins were identified in the iTRAQ-HNECs-Virus dataset. **A** Heat map showing the relative abundance of 89 proteins (FC > 1.125, $p < 0.05$). The color key indicates the relative abundance of each protein (-2 to 2) across eight samples. **B** Volcano plot demonstrates fold changes in protein abundance between Mock and Virus-only group. The x -axis represents the log₂ ratio, and the y -axis represents significant differences (-log₁₀ of p -value). **C** Significant biological pathways enriched among 89 proteins identified via iTRAQ are represented as bar graphs ($p < 0.05$) **D** Pie graph showing

the CD47-included top 5 biological processes in functional annotation with gene ontology (GO) analysis: *response to stimulus-related* consists of GO:0009605-response to external stimulus, GO:0006952-defense response, GO:0009607-response to biotic stimulus, GO:0043207-response to external biotic stimulus, GO:0051707-response to other organism, GO:0080134-regulation of response to stress, GO:0048584-positive regulation of response to stimulus, GO:0031347-regulation of defense response, GO:0032101-regulation of response to external stimulus, GO:0009617-response to bacterium, and GO:0031349-positive regulation of defense response; *Cell migration-related* consists of GO:0040011-locomotion, GO:0006928-movement of cell or subcellular component, GO:0048870-cell motility, GO:0051674-localization of cell, GO:0016477-cell migration, and GO:0098602-single organism cell adhesion; *Immune system process-related* consists of GO:0002682-regulation of immune system process, GO:0002252-immune effector process, and GO:0002684-positive regulation of immune system process; GO:0007166-cell surface receptor signaling pathway; and GO:0051128-regulation of cellular component organization.

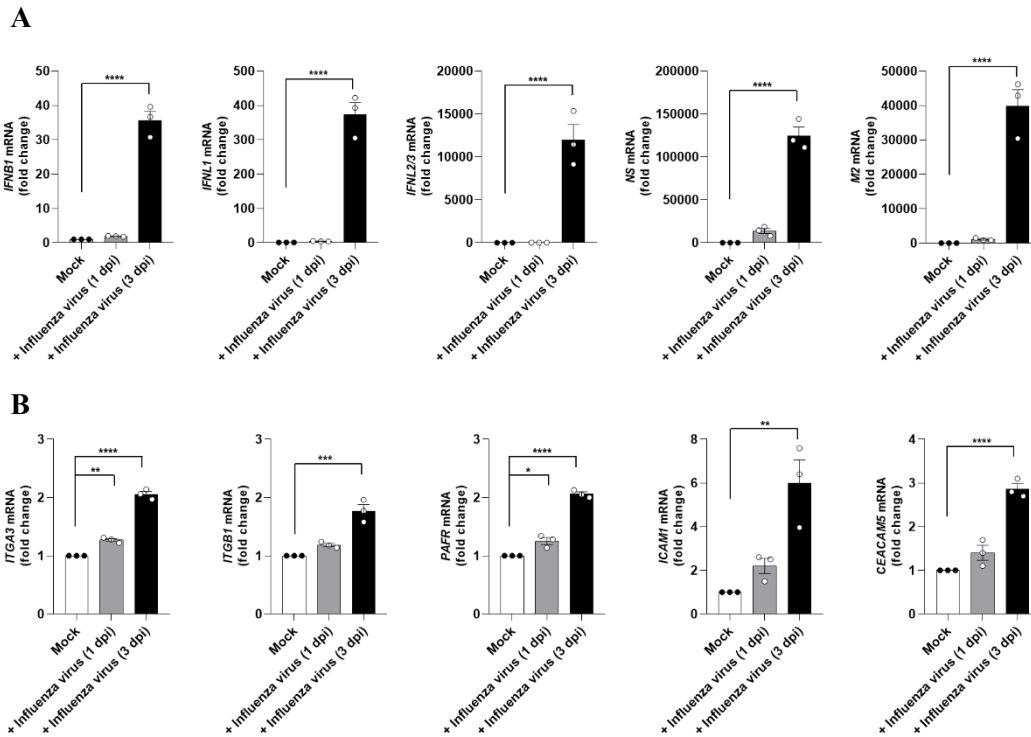


Figure 2. Gene expression profiles during influenza virus infection. A-B qPCR analysis of host cell and viral genes at 1 and 3 dpi ($n = 3$). Results are the means \pm SEM; $*p < 0.05$; $**p < 0.01$; $***p < 0.001$; $****p < 0.0001$ by one-way ANOVA with Turkey's multiple comparisons test. *IFNB1*, type I interferon; *IFNL1* and *IFNL2/3*, type III interferons; *M2*, influenza matrix protein 2; *NS1*, influenza non-structural protein 1; *PAFR*, platelet activating factor receptor; *CECAM5*, carcinoembryonic antigen-related cell adhesion molecule 5; *ICAM1*, Intercellular adhesion molecule 1 and *ITGA3* and *ITGB1*, integrins alpha 3 and beta 1.

2. NF- κ B/IFN signalling pathway-dependent CD47 expression in HBECs upon influenza virus infection

Given that CD47 is transcriptionally regulated by nuclear factor kappa B (NF- κ B) in a hepatocellular carcinoma mouse model⁴⁰, I examined whether airway epithelial CD47 is regulated by the NF- κ B pathway. In HBECs, I confirmed the activation of the NF- κ B pathway induced by viral infection, evidenced by p65 phosphorylation at 1 h post-infection (hpi), along with the induction of the downstream target protein, intercellular adhesion molecule-1 (ICAM-1)^{19,23}. CD47 protein abundance slightly increased after 1 hpi and reached its peak at 12 hpi (Figure 3A). Pre-treatment of HBECs with caffeic acid phenethyl ester (CAPE), a specific inhibitor of NF- κ B, resulted in the inhibition of viral infection-induced p65 phosphorylation at 1 hpi (Figure 3B). Additionally, the upregulation of ICAM-1 and CD47 at 24 hpi was blocked (Figure 4D), confirming that the role of NF- κ B pathway in influencing CD47 upregulation in airway epithelial cells during viral infection. I also conducted an extensive investigation to determine whether CD47 induction is dependent on IFN, the production of which is NF- κ B-dependent⁴¹. I observed an increase in CD47 expression following viral infection (Figure 3C and 3D), and this effect was replicated in HBECs treated with recombinant human IFN- β (Figure 3E) and IFN- λ 1 (Figure 3F). Notably, the induction of CD47 by influenza virus was entirely suppressed when anti-IFNAR (Figure 3C) or anti-IFNLR (Figure 3D) neutralizing antibodies were applied. Additionally, the induction of CD47 by recombinant human IFN- β was effectively inhibited by anti-IFNAR neutralizing antibodies (Figure 3E), while CD47 induction by recombinant human IFN- λ 1 was specifically blocked by anti-IFNLR neutralizing antibodies (Figure 3F). These results collectively demonstrate that CD47 induction occurs via the NF- κ B/IFN pathway.

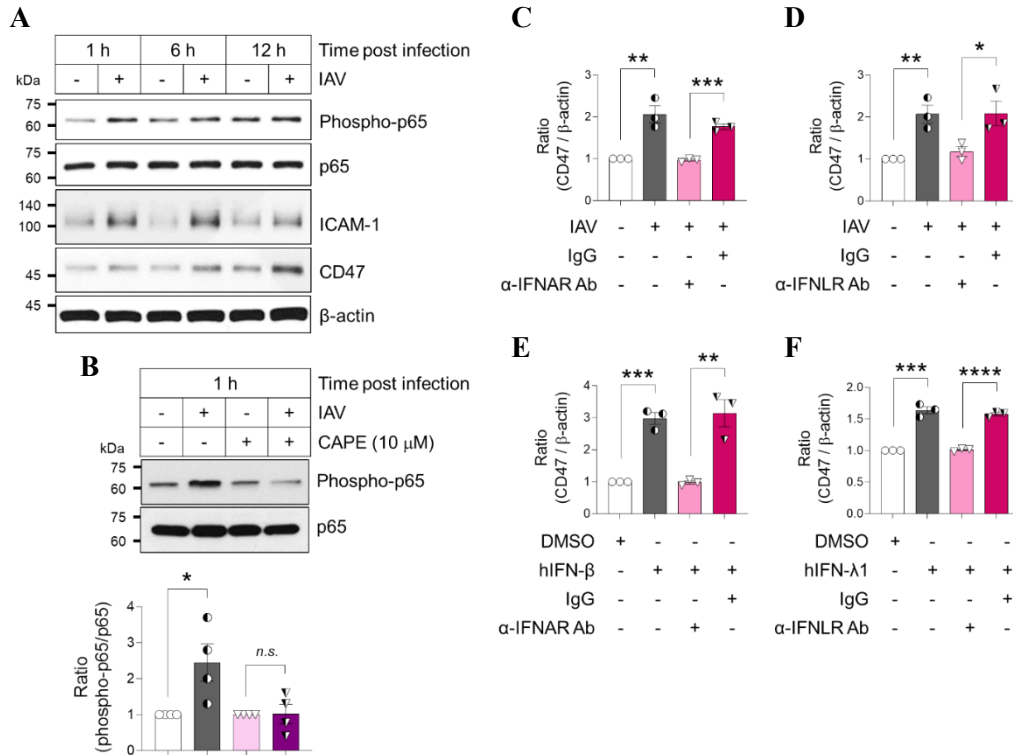


Figure 3. Viral infection-induced CD47 expression via NF- κ B/IFN signalling pathway. **A** HBECs were infected with influenza virus and harvested at 1, 6, and 12 h after viral infection. Note that these blots represent one of three independent experiments. **B** HBECs were treated with or without 10 μ M of NF- κ B inhibitor caffeic acid phenethyl ester (CAPE) for 1 h before influenza virus infection. Immunoblot analysis of phospho-p65, p65, ICAM-1, and CD47 in the indicated time ($n = 4$). **C-F** HBECs were infected with influenza virus (**C** and **D**), and with recombinant human IFN- β (**E**) or IFN- λ 1 (**F**). CD47 protein expression was analyzed by immunoblotting after pretreating the cells with either IgG or α -IFNAR Ab (**C** and **E**) or α -IFNLR Ab (**D** and **F**) ($n = 3$). Results are presented as the mean \pm SEM; * $p < 0.05$; ** $p < 0.01$; *** $p < 0.001$; **** $p < 0.0001$ using Student's t -test. *n.s.*, not significant.

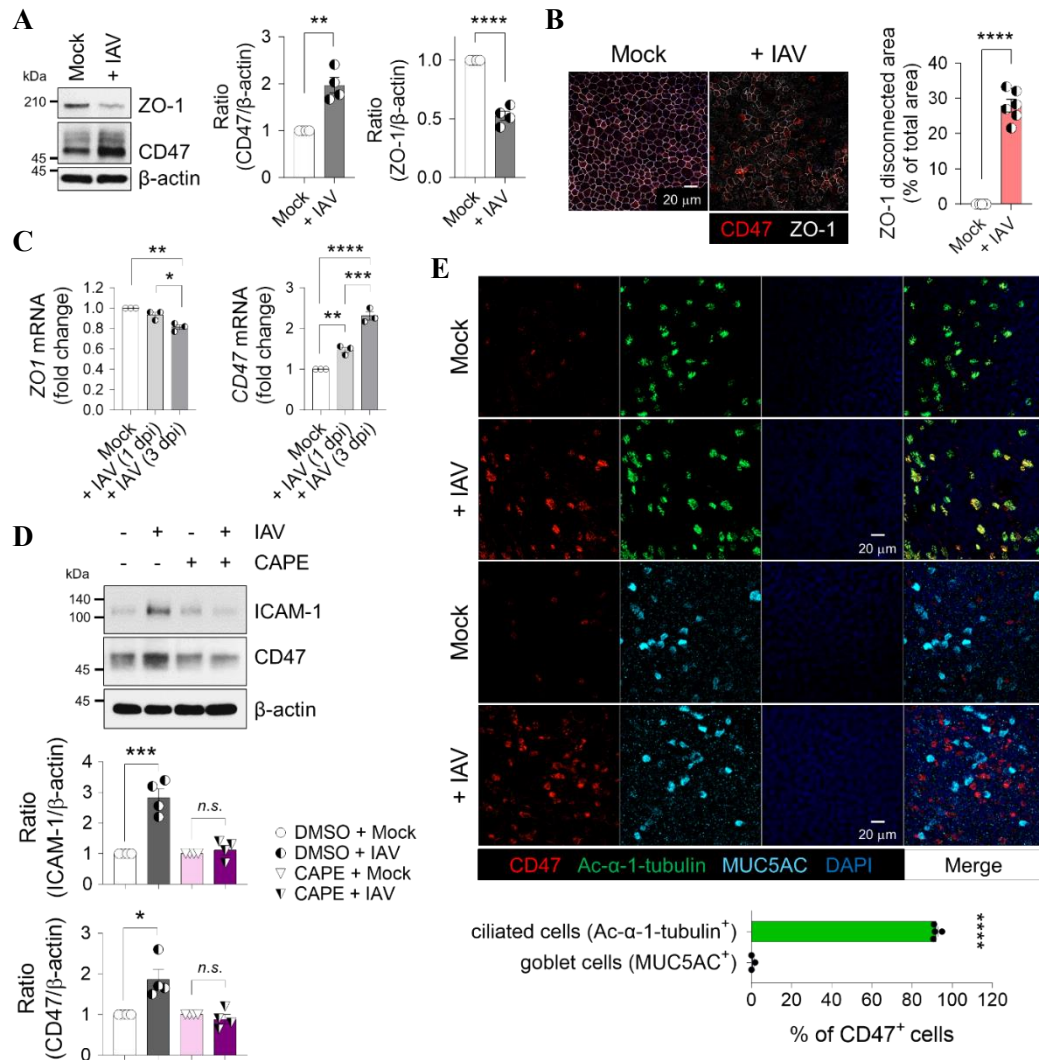


Figure 4. Influenza virus induces CD47 expression on the apical surface of ciliated cells in an NF- κ B-dependent manner. HBECs were infected with (+ *IAV*) or without (*Mock*) influenza A virus. **A** Immunoblot analysis of junction protein ZO-1 and surface protein CD47 at 1-day post-infection (dpi). Normalized CD47 and ZO-1 protein levels are presented as bar graphs (*Mock*, $n = 4$; + *IAV*, $n = 4$). **B** Representative whole-mount images of ZO-1 (white) and CD47 (red) at 1 dpi. The area where ZO-1 disconnection occurred are

presented as bar graphs (Mock, $n = 6$; + IAV, $n = 6$). **C** Quantitative PCR (qPCR) analysis of *ZO-1* and *CD47* mRNAs at 1 and 3 dpi [Mock, $n = 3$; + IAV (1 dpi), $n = 3$; + IAV (3 dpi), $n = 3$]. **D** HBECs were treated with or without 10 μ M NF- κ B inhibitor caffeic acid phenethyl ester (CAPE) for 1 h before influenza virus infection. Immunoblot analysis of ICAM-1 and CD47 at 1 dpi. Normalized ICAM-1 and CD47 protein levels are presented as bar graphs (DMSO + Mock, $n = 4$; DMSO + IAV, $n = 4$; CAPE + Mock, $n = 4$; CAPE + IAV, $n = 4$). **E** Whole-mount images of influenza virus-infected HBECs. Co-staining of CD47 (red) and ciliated cell-specific marker protein Ac- α -tubulin (green, $n = 4$) or goblet cell-specific marker protein MUC5AC (cyan, $n = 3$). Percentages of CD47-positive cells are presented as bar graphs. Results are shown as the mean \pm SEM; * $p < 0.05$; ** $p < 0.01$; *** $p < 0.001$; **** $p < 0.0001$ using one-way ANOVA with Tukey's multiple comparisons test or Student's *t*-test. *n.s.*, not significant.

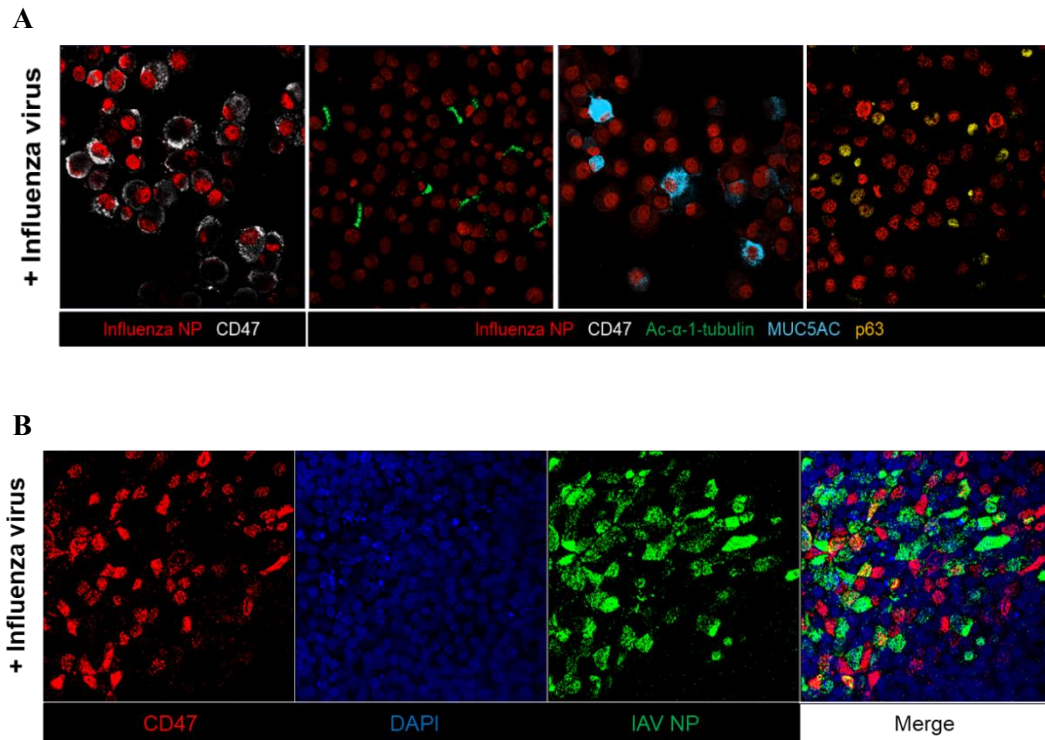


Figure 5. Characterization of CD47 induction in the influenza virus-infected HBECs. HBECs were infected with (+ *IAV*) influenza A virus. **A** Cytospin immunofluorescence staining of influenza virus-infected HBECs at 1 dpi. Co-staining of CD47 (white), Influenza virus nucleoprotein (NP) (red), ciliated cell-specific marker protein Ac- α -tubulin (green), goblet cell-specific marker protein MUC5AC (cyan), and basal cell-specific marker protein p63 (yellow). **B** Whole-mount images of influenza virus-infected HBECs at 1 dpi. Co-staining of CD47 (red), Influenza virus Nucleoprotein (NP) (green), and DAPI (blue). All images shown were representative of three independently performed experiments.

3. CD47 is upregulated and localized to the apical surface of ciliated cells following infection of HNECs and HBECs with influenza virus

To ascertain if viral infection-induced CD47 expression is specific to certain cell types, I conducted co-immunostaining of airway epithelial cells and observed that CD47⁺ HNECs (Figure 6D) and HBECs (Figure 4E) were co-localized with the ciliated cell-specific marker, Ac- α -tubulin ($92.0 \pm 1.0\%$ in HNECs; $91.1 \pm 0.6\%$ in HBECs) rather than the goblet cell-specific marker, MUC5AC ($0.6 \pm 0.6\%$ in HNECs; $3.0 \pm 1.6\%$ in HBECs), during viral infection. Interestingly, co-immunostaining of CD47 and influenza nucleoprotein (NP) revealed that not all CD47-positive cells completely overlapped with viral protein (Figure 5B). It's worth noting that ciliated cells are a part of the epithelium, lining the apical surface of the respiratory tract and exposing their cilia to the lumen⁴². Therefore, the detection of CD47 co-expressed with Ac- α -tubulin indicates that it is present on the apical side of the ciliated cells. In a similar context, the analysis of HNEC single-cell RNA sequencing (scRNA-seq) data revealed that CD47⁺ clusters primarily consist of FOXJ1⁺ cells, with a notable prevalence of deuterosomal cells and a partial presence of multiciliated cells (Figure 6E)⁴³. To validate these findings in HBECs, I analyzed two publicly available scRNA-seq datasets performed with HBECs. My analysis revealed that CD47 expression is predominantly expressed in FoxJ1⁺ cells, encompassing deuterosomal cells, and to a lesser extent, multi-ciliated cells within HBECs (Figure 7A and 7B)⁷¹. These results reinforce a fundamental aspect of this study, underscoring the specific presence of CD47 expression in ciliated epithelial cells. Fluorescence-activated cell sorting (FACS) analysis further confirmed the presence of CD47 protein on the cell surface of HNECs, with increased expression observed during viral infection (Figure 6F). Therefore, these findings demonstrate that CD47 is induced and exposed on the apical surface of ciliated cells in respiratory epithelial cells infected with the influenza virus.

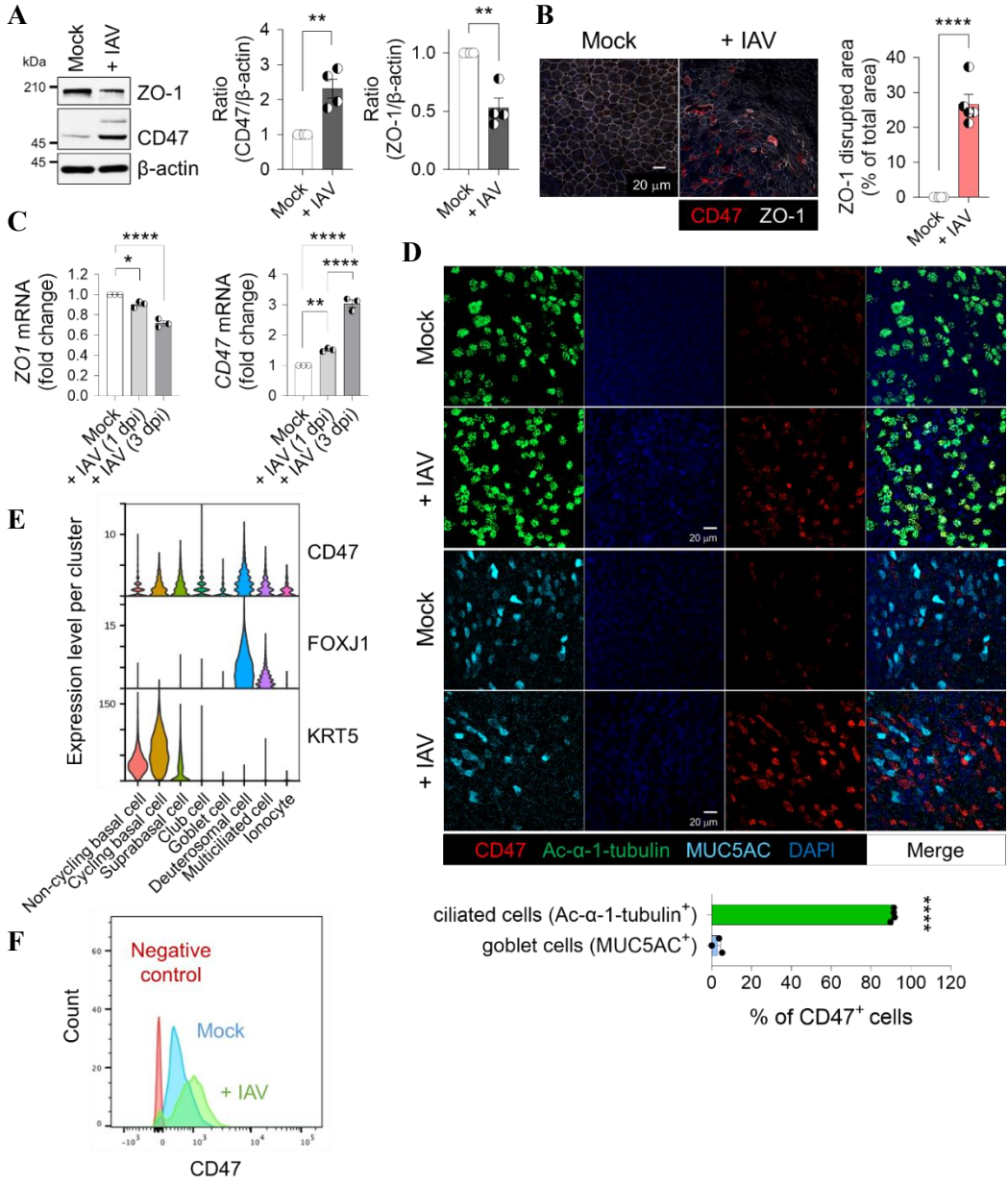
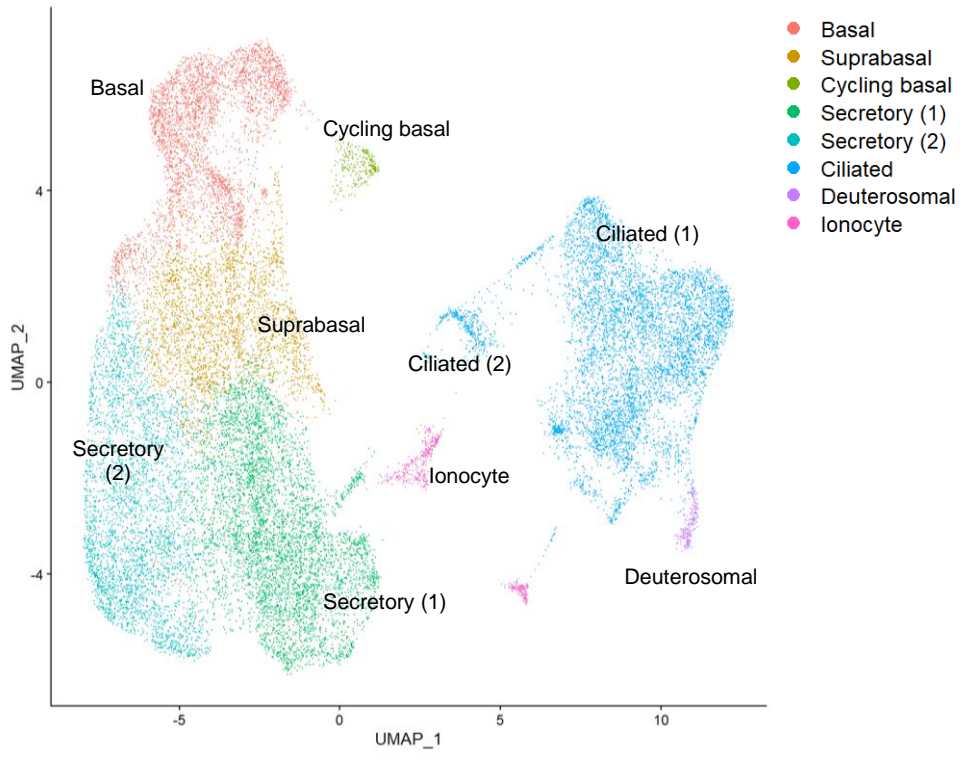


Figure 6. CD47 induction and exposure in the apical surface of ciliated HNECs following influenza virus infection. HNECs were infected with (+ *IAV*) or without (*Mock*)

influenza virus. **A** Immunoblot analysis of junction protein Zona occluden-1 (ZO-1) and surface protein CD47 at 1 dpi. Normalized CD47 protein levels are presented as bar graphs ($n = 4$). **B** Representative whole-mount images of ZO-1 (white) and CD47 (red) at 1 dpi. The area where ZO-1 disconnection occurred are depicted as bar graphs ($n = 5$). **C** Quantitative PCR (qPCR) analysis of *ZO-1* and *CD47* mRNAs at 1 and 3 dpi ($n = 3$). **D** Whole-mount images of influenza virus-infected HNECs. Co-staining of CD47 (red) and ciliated cell-specific marker protein Ac- α -tubulin (green) or goblet cell-specific marker protein MUC5AC (cyan). Percentages of CD47-positive cells were presented as bar graphs ($n \geq 3$). **E** Expression of *CD47*, ciliated cell-specific marker *FoxJ1*, and basal cell-specific marker *KRT5* are presented as violin graphs based on the scRNA-seq of ALI-cultured HNECs (14 days). **F** Flow cytometry analysis of CD47 expression in the surface of HNECs at 1 dpi. Results are shown as the mean \pm SEM; * $p < 0.05$; ** $p < 0.01$; **** $p < 0.0001$ using one-way ANOVA with Tukey's multiple comparisons test or Student's *t*-test.

(22,189 cells, Dimension 20, resolution 0.3 (Ravindra NG, et al. PLoS Biol. 2021))

A



B

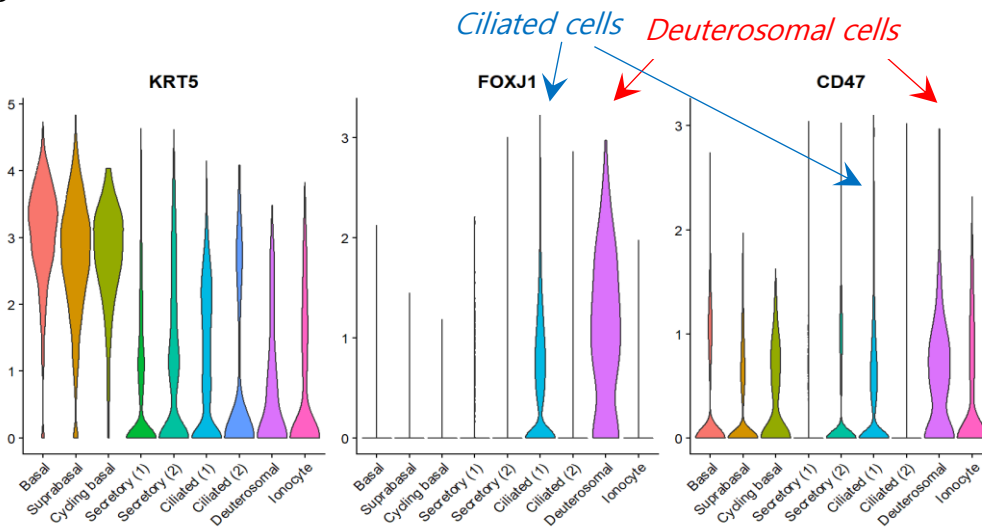


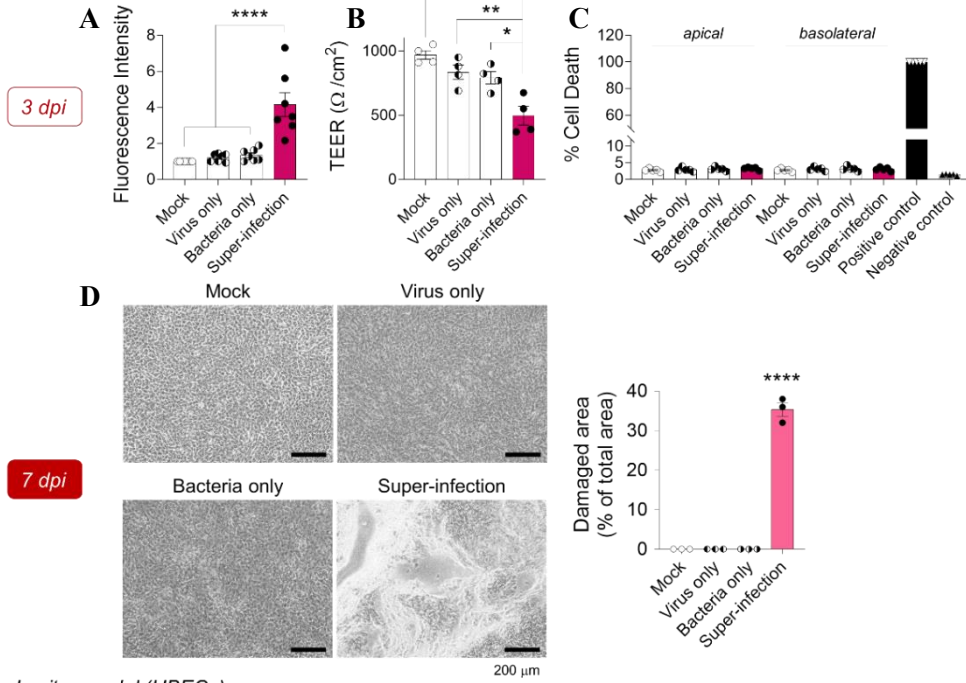
Figure 7. Publicly available single-cell RNA sequencing (scRNA-seq) data of human bronchial epithelial cells. Re-analysis of publicly available scRNA-seq datasets of human bronchial epithelial cells. **A** Uniform manifold approximation and projection (UMAP) plots of human bronchial epithelial cells. **B** Violin plot showing expression of *CD47*, ciliated cell-specific marker *FOXJ1*, and basal cell-specific marker *KRT5* in each cell cluster.

4. Epithelial CD47 in HBECs and HNECs facilitates super-infection

To elucidate the mechanisms underlying susceptibility to secondary bacterial infection induced by viral infection, I developed an in vitro model of super-infection using HNECs and HBECs (Figure 8). HNECs simulate the upper airway, the initial site of viral infection, while HBECs represent the lower airway, where super-infection has a terminal impact. Following air–liquid interface (ALI) culture for 14 days (HNECs) or 21 days (HBECs), cells were infected with influenza virus pH1N1 and/or *S. aureus*. Since ZO-1 displayed reduced levels and disconnection during viral infection, I assessed the impact of secondary bacterial infection on HNECs and HBECs by evaluating paracellular permeability, changes in cellular morphology, and cell viability. When cells were co-infected with virus (MOI 1) and bacteria (MOI 5 for HNECs; MOI 3 for HBECs), paracellular permeability of fluorescein isothiocyanate (FITC)-dextran was significantly elevated (Figure 8A and 8E), and trans-epithelial electrical resistance (TEER) showed a substantial decrease (Figure 8B and 8F), as compared to mock-infected HNECs and HBECs. Notably, both of these parameters remained unchanged in cells subjected to either virus or bacteria single infection. Although no significant detrimental effect of super-infection was observed in lactate dehydrogenase (LDH) assay at 3 dpi (Figure 8C and 8G), visible cytopathogenic effects resulting from super-infection became apparent after 7 days in HNECs and 5 days in HBECs (Figure 8D and 8H). Given that HNECs exhibited greater resistance to super-infection compared to HBECs⁴⁴, it necessitated a longer incubation period with bacteria to observe a similar super-infection effect in HBECs. To investigate the function of CD47 in viral–bacterial super-infection, I reduced CD47 expression by transfecting airway epithelial cells with lentiviral shRNA targeting the *CD47* gene. This resulted in a decrease in *CD47* transcript levels to $56.1 \pm 4.4\%$ in HNECs (Figure 9A) and $58.6 \pm 3.6\%$ in HBECs (Figure 10A), accompanied by a corresponding reduction in CD47 protein levels, $41.7 \pm 5.2\%$ in HNECs (Figure 9B) and $54.2 \pm 6.3\%$ in HBECs (Figure 10B). Subsequently, I assessed the impact of *CD47* knockdown on the response to super-infection by measuring paracellular FITC-dextran permeability and TEER, which revealed a substantial attenuation of these

effects in both HNECs (Figure 9C and 9D) and HBECs (Figure 10C and 10D) following *CD47* shRNA treatment. Furthermore, I inhibited *CD47* protein function by pre-incubating cells with α -h*CD47* neutralizing antibodies before super-infection. This intervention resulted in significant mitigation of disruption in paracellular permeability and TEER at 3 dpi in HNECs (Figure 9E and 9F) and HBECs (Figure 10C and 10D), as well as a reduction in the cytopathogenic effects of super-infection in HNECs at 7 dpi (Figure 9G) and HBECs at 5 dpi (Figure 10E). In a super-infection model with *S. pneumoniae*, the treatment of *CD47* shRNA and α -h*CD47* antibodies exhibited comparable protective effects on paracellular permeability and TEER in HBECs (Figure 11A and 11B). These results suggest that viral infection-induced epithelial *CD47* may be exploited by pathogenic bacteria to induce super-infection by disrupting cellular junction integrity.

In vitro model (HNECs)



In vitro model (HBECs)

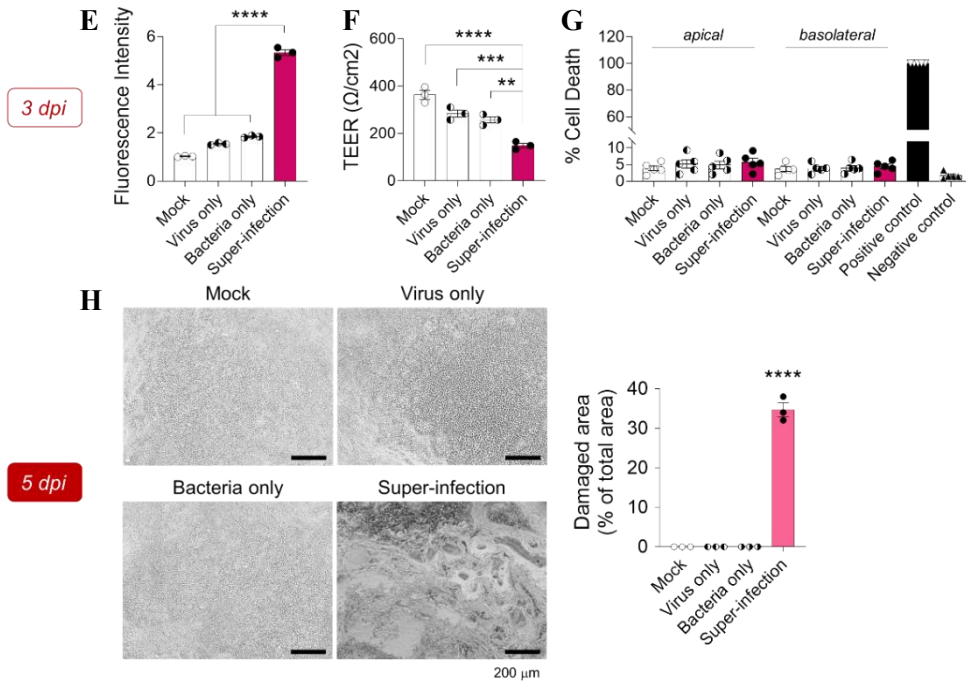


Figure 8. In-vitro model of super-infection used in this study. **A-H** In-vitro super-infection models in HNECs (**A-D**) and HBECs (**E-H**). The ratio of paracellular FITC-dextran permeability (**A** and **E**), trans-epithelial electrical resistance (**B** and **F**), and LDH levels of apical or basolateral fractions (**C** and **G**) measured in non-infected (*Mock*), influenza virus-infected (*Virus only*, MOI 1), *S. aureus*-infected (*Bacteria only*, MOI 5 for HNECs or MOI 3 for HBECs), and viral-bacterial co-infected cells (*Super-infection*) ($n \geq 3$). Microscopic images show morphological changes of HNECs at 7 dpi (**D**) and HBECs at 5 dpi (**H**). The percentage of the damaged area is presented as bar graphs ($n = 3$). Results are shown as the mean \pm SEM; * $p < 0.05$; ** $p < 0.01$; *** $p < 0.001$; **** $p < 0.0001$ using one-way ANOVA with Tukey's multiple comparisons test.

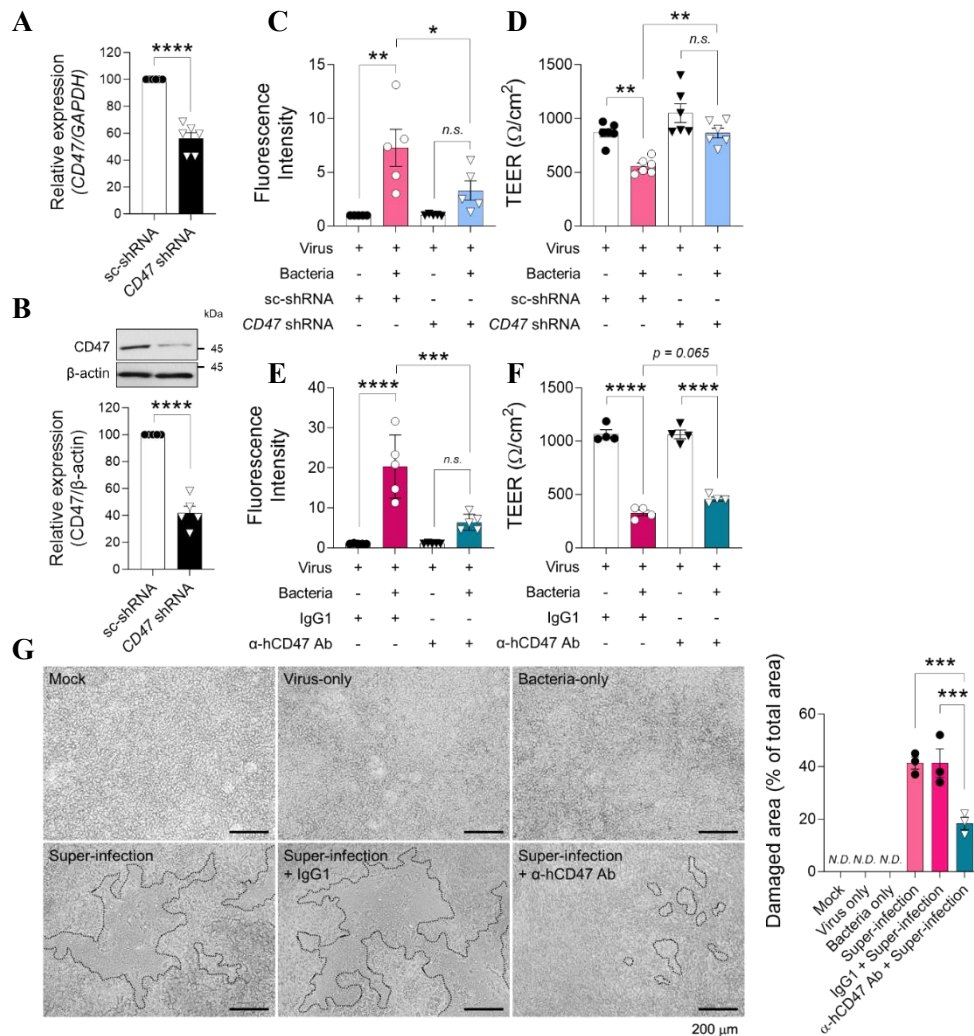


Figure 9. Protective effect of knock-down and neutralization of CD47 on super-infection in HNECs. For *CD47* knock-down, HNECs were transfected with scrambled shRNA (*sc-shRNA*) or shRNA targeting *CD47* (*CD47 shRNA*) using a lentiviral delivery system. For *CD47* neutralization, HNECs were treated with either IgG1 (MOPC-21) or α -hCD47 (B6H12.2) antibodies. **A** Gene expression of *CD47* was analyzed using qRT-PCR (normalized by *GAPDH* mRNA) ($n = 6$). **B** Protein expression of *CD47* was analyzed via

immunoblotting (normalized by β -actin). Normalized CD47 protein levels are presented as bar graphs ($n = 5$). **C-F** Paracellular FITC-dextran permeability ($n = 5$) (**C**, **E**) and trans-epithelial resistance ($n \geq 4$) (**D**, **F**) of virus only and super-infection groups were measured in the presence of either *CD47* shRNA or α -hCD47 antibodies. **G** Microscopic images of HNECs at 7 dpi. The damaged area is depicted in dotted lines and the percentage of the damaged area is presented as bar graphs ($n = 3$). Results are shown as the mean \pm SEM; * $p < 0.05$; ** $p < 0.01$; *** $p < 0.001$; **** $p < 0.0001$ using Student's *t*-test or one-way ANOVA with Tukey's multiple comparison test. *n.s.*, not significant.

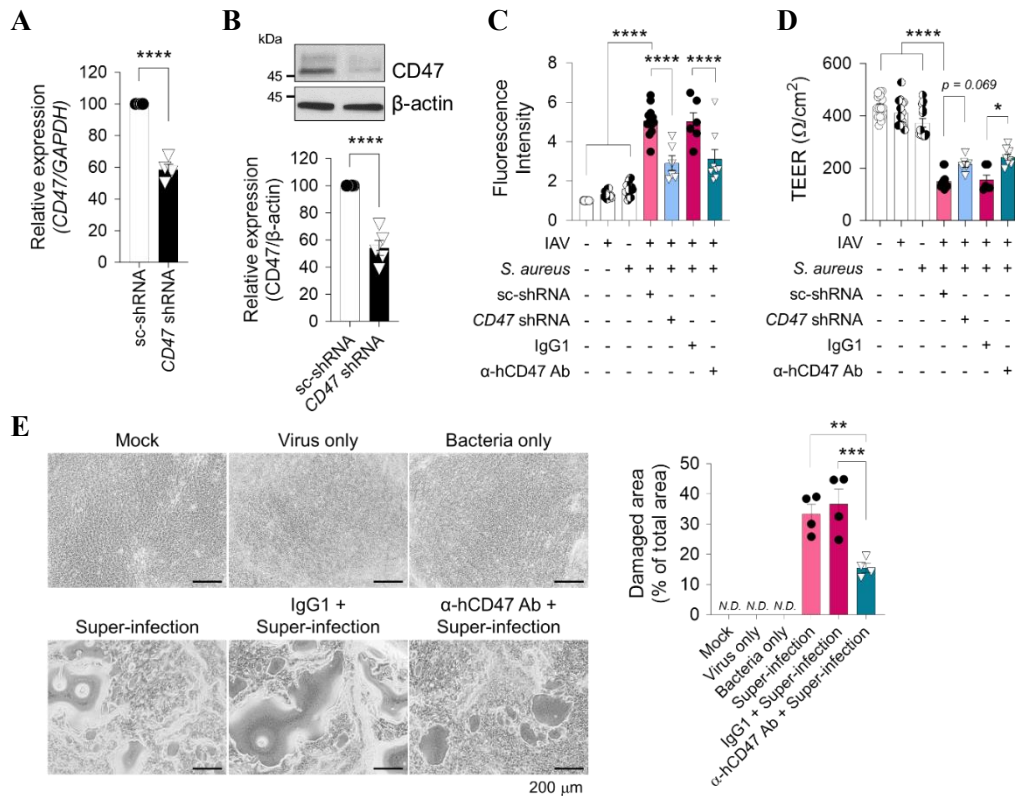


Figure 10. Knock-down and neutralization of CD47 protects HBECs from viral-bacterial co-infection. For *CD47* knock-down, HBECs were transfected with scrambled shRNA (*sc-shRNA*) or shRNA targeting *CD47* (*CD47 shRNA*) using a lentiviral delivery system. For *CD47* neutralization, HBECs were treated with either IgG1 (MOPC-21) or α-hCD47 (B6H12.2) antibodies. **A** Gene expression of *CD47* was analyzed using qRT-PCR (normalized by *GAPDH* mRNA) (*sc-shRNA*, $n = 4$; *CD47 shRNA*, $n = 4$). **B** Protein expression of *CD47* was analyzed using immunoblotting (*sc-shRNA*, $n = 5$; *CD47 shRNA*, $n = 5$). **C** Paracellular FITC-dextran permeability was measured in Mock ($n = 16$), Virus only (IAV, $n = 16$), Bacteria only (*S. aureus*, $n = 16$), *sc-shRNA* + Super-infection ($n = 12$), *CD47 shRNA* + Super-infection ($n = 6$), IgG1 + Super-infection ($n = 6$), and α-hCD47 antibodies (Ab) + Super-infection ($n = 8$). **D** Trans-epithelial resistance was measured in

Mock ($n = 15$), IAV ($n = 14$), *S. aureus* ($n = 13$), sc-shRNA + Super-infection ($n = 13$), CD47 shRNA + Super-infection ($n = 6$), IgG1 + Super-infection ($n = 6$), and α -hCD47 Ab + Super-infection ($n = 8$). **E** Microscopic images of HBECs at 5 dpi. The percentage of the damaged area is presented as bar graphs (Mock, $n = 3$; Virus only, $n = 3$; Bacteria only, $n = 3$; Super-infection, $n = 4$; IgG1 + Super-infection, $n = 4$; α -hCD47 Ab + Super-infection, $n = 4$). Results are shown as the mean \pm SEM; * $p < 0.05$; ** $p < 0.01$; *** $p < 0.001$; **** $p < 0.0001$ using Student's *t*-test or one-way ANOVA with Tukey's multiple comparisons test. *N.D.*, not determined.

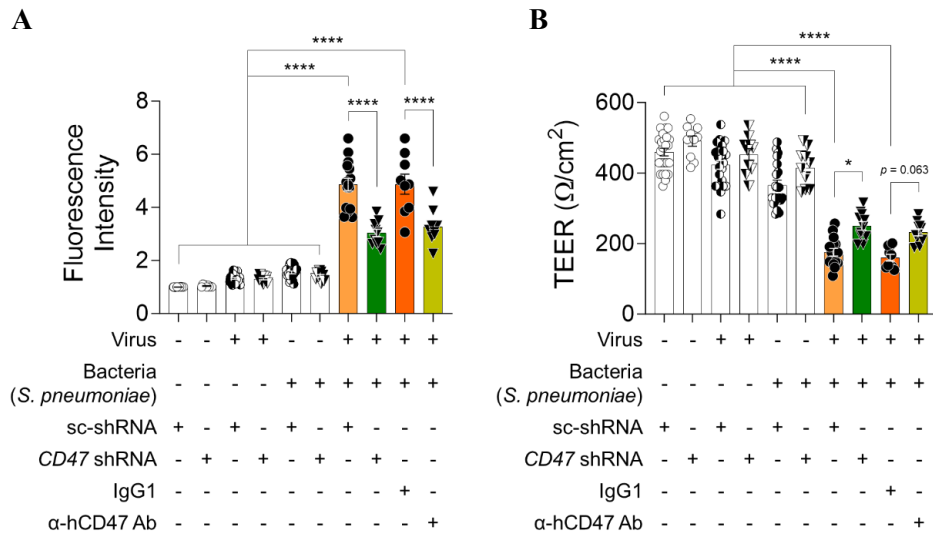


Figure 11. Protective effect of knock-down and neutralization of CD47 on the *S. pneumoniae*-mediated super-infection in HBECs. **A, B** For *CD47* knock-down, HBECs were transfected with scrambled shRNA (*sc-shRNA*) or shRNA targeting *CD47* (*CD47 shRNA*) using a lentiviral delivery system. For *CD47* neutralization, HBECs were treated with either IgG1 (MOPC-21) or α -hCD47 (B6H12.2) antibodies. Paracellular FITC-dextran permeability (**A**) and trans-epithelial resistance (**B**) of virus-only, bacteria-only, and super-infection groups were measured in the presence of *sc-shRNA*, *CD47 shRNA*, IgG1, or α -hCD47 antibodies ($n \geq 10$). Results are the mean \pm SEM; * $p < 0.05$; **** $p < 0.0001$ using one-way ANOVA with Tukey's multiple comparisons test.

5. Direct interactions between epithelial CD47 and the bacterial FnBP in viral-bacterial co-infected cells

With the exception of live *S. aureus*, no other factors, such as *S. aureus*-cultured media supernatant containing secreted proteins or extracellular vesicles (*M*), UV-killed *S. aureus* with intact structural proteins (*U*), or heat-killed *S. aureus* with denatured proteins (*H*), disrupted paracellular FITC-dextran permeability of HBECs infected with influenza virus (Figure 12A). A whole-mount image of viral-infected HBECs briefly exposed to *S. aureus* (for 3 hours, as longer exposure led to cell layer destruction) revealed the co-localization of bacteria with CD47 on the cell surface where ZO-1 disruption occurred (Figure 13C). This observation led to my hypothesis that live *S. aureus* directly interacts with host CD47 to cause super-infection. To validate this hypothesis, I initially performed a bacterial adhesion assay to quantify the number of bacteria adhering to HBECs after a 3-hour co-incubation. This analysis revealed a significant increase in the adherence of *S. aureus* to the cells following viral infection in HBECs (Figure 13D). Additionally, the virus-induced bacterial adherence was inhibited when the cells were pre-incubated with α -hCD47 antibodies (Figure 13D), suggesting that this cell-to-bacteria interaction may be depend on CD47. In my preliminary study, designed to elucidate the mechanistic basis how bacteria causing pneumonia following a secondary bacterial infection bind to CD47, I examined whether other pneumonia-causing bacteria bind to CD47. This was assessed by testing the adhesion of *S. pneumoniae*, *Pseudomonas aeruginosa* and *S. aureus* on A549 cells, with the commensal bacterium, *Staphylococcus epidermidis* serving as a negative control. The results showed that adherence of pneumonia-causing gram-positive bacteria *S. aureus* and *S. pneumoniae* to cellular CD47 was significantly inhibited following pre-incubation of the cells with α -hCD47 antibodies. However, adherence of pneumonia-causing gram-negative bacterium *P. aeruginosa*, was not affected by α -hCD47 antibodies. Moreover, the gram-positive commensal bacterium, *S. epidermidis*, did not bind to the cells (Figure 12B). Since only *S. aureus* and *S. pneumoniae* showed CD47-specific binding, I hypothesized that these two pathogens might share CD47-interacting components. Literature indicated that during

infection, *S. aureus* and *S. pneumoniae* utilize structurally homologous adhesion molecules, such as Fn-binding protein (FnBP), to interact with integrin $\alpha 5\beta 1$ by using Fn as a bridge. Specifically, FnBP A or B of *S. aureus* and pneumococcal adherence and virulence factor A (PavA) of *S. pneumoniae* are involved in these interactions^{4,45,46}. To test whether FnBPs are required for *S. aureus* binding to CD47, I employed *S. aureus* laboratory strain 8325-4 (FnBP A+/B+) and three mutant strains (FnBP A+/B-, A-/B+, and A-/B-)⁴⁷. In bacterial adhesion assay, I observed that the single deletion of FnBP A or B reduced *S. aureus* adherence by $23.7 \pm 1.7\%$ or $24.7 \pm 2.9\%$, respectively, while the double deletion of FnBP A and B synergically decreased adherence by $35.9 \pm 2.4\%$ (Figure 13E). In contrast to the FnBP A+/B+ strain, where adherence to the viral infection-induced CD47 was inhibited by α -hCD47 antibodies in a concentration-dependent manner (Figure 13F), the double deletion mutant strain (FnBP A-/B-) showed less adherence to viral infection-induced CD47, and this adherence was not affected by CD47 blocking (Figure 13G). These findings indicated that FnBP A+/B+ binds to the surface of HBECs through CD47-specific ($26.4 \pm 1.9\%$) or non-specific interaction ($73.6 \pm 1.0\%$), whereas FnBP A-/B- only by non-specific interaction ($61.8 \pm 2.6\%$), suggesting a partial but direct interaction between CD47 and FnBP. To further support my hypothesis, I established an in vitro pull-down assay in which *S. aureus* was incubated with recombinant His-tagged hCD47 proteins and then pulled down using α -His-Dynabeads. My results indicated a substantial increase in the precipitation of *S. aureus* in the pellets and a decreased presence in the supernatants when recombinant hCD47 was present, compared to the condition in which hCD47 was absent (Figure 12C), confirming that *S. aureus* directly binds to CD47. Lastly, to validate the direct interaction between CD47 and FnBP, I performed a pull-down assay using FnBP A+/B+ and FnBP A-/B-. My results demonstrated that significantly less FnBP A-/B- ($15.8 \pm 6.9\%$) was precipitated in the pellets, even in the presence of recombinant hCD47, in contrast to FnBP A+/B+ ($83.2 \pm 5.7\%$) (Figure 13H). By conducting in vitro pull-down assay using five *S. aureus* mutant strains, in which cell wall-anchored proteins were deleted; *fnbB::Tn* ($\Delta fnbB$), *sasG::Tn* ($\Delta sasG$), *isdB::Tn* ($\Delta isdB$), *sdrE::Tn* ($\Delta sdrE$), and *clfA::Tn* ($\Delta clfA$). I

confirmed that only FnBP mediates the interaction between *S. aureus* and CD47 (Figure 12D and 12E). This observation supports the conclusion that *S. aureus* directly binds to HBECs through a specific interaction between FnBP and CD47.

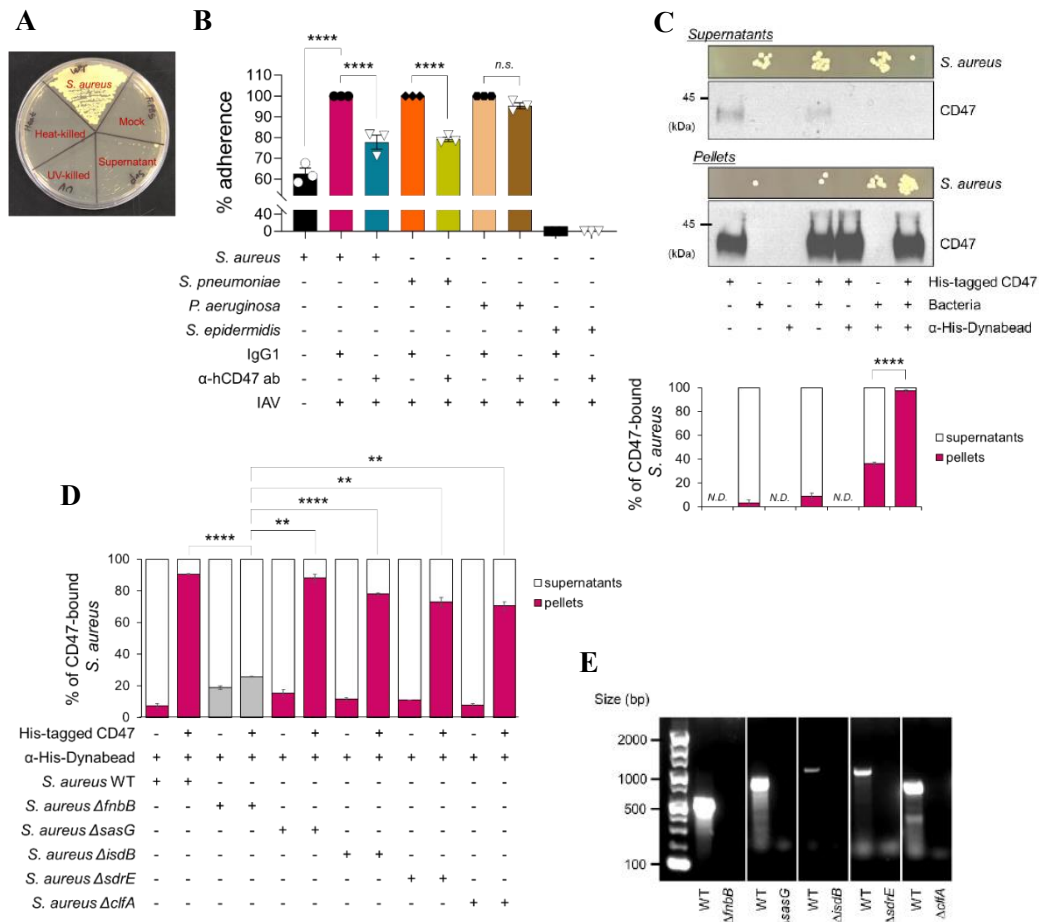


Figure 12. Direct interactions between epithelial CD47 and *S. aureus*. **A** Bacterial plating of live *S. aureus* or *S. aureus*-derived samples (*S*, supernatant of *S. aureus*-cultured media; *U*, UV-killed *S. aureus*; *H*, heat-killed *S. aureus*). **B** Bacterial adhesion assay. Adherence of *S. aureus* (gram-positive), *S. pneumoniae* (gram-positive), *P. aeruginosa* (gram-negative), and *S. epidermidis* (gram-positive, commensal bacterium), was assessed in the influenza-infected A549 cells. The cells were treated with IgG1 control antibodies or α -hCD47 neutralizing antibodies (2 h), followed by bacterial infection (MOI 10) for 3 h ($n = 3$). **C** Pull-down assay using His-tagged hCD47 recombinant protein. Bacterial plating and immunoblot analysis were performed using supernatants and pellets after separation

with α -His-DynabeadsTM/DynaMagTM-2 system. The graphs present the percentage of colony numbers grown in the culture of the supernatants or the pellets ($n = 3$). **D** In-vitro pull-down assay of WT and five cell wall-anchored proteins (CWAs) deletion mutants of *S. aureus*; *fnbB::Tn* ($\Delta fnbB$), *sasG::Tn* ($\Delta sasG$), *isdB::Tn* ($\Delta isdB$), *sdrE::Tn* ($\Delta sdrE$), and *clfA::Tn* ($\Delta clfA$) ($n = 3$). **E** Gene deletions were validated by PCR. Results are shown as mean \pm SEM; ** $p < 0.01$; **** $p < 0.0001$ using one-way ANOVA with Tukey's multiple comparisons test or Student's *t*-test. *N.D.*, not determined. *n.s.*, not significant.

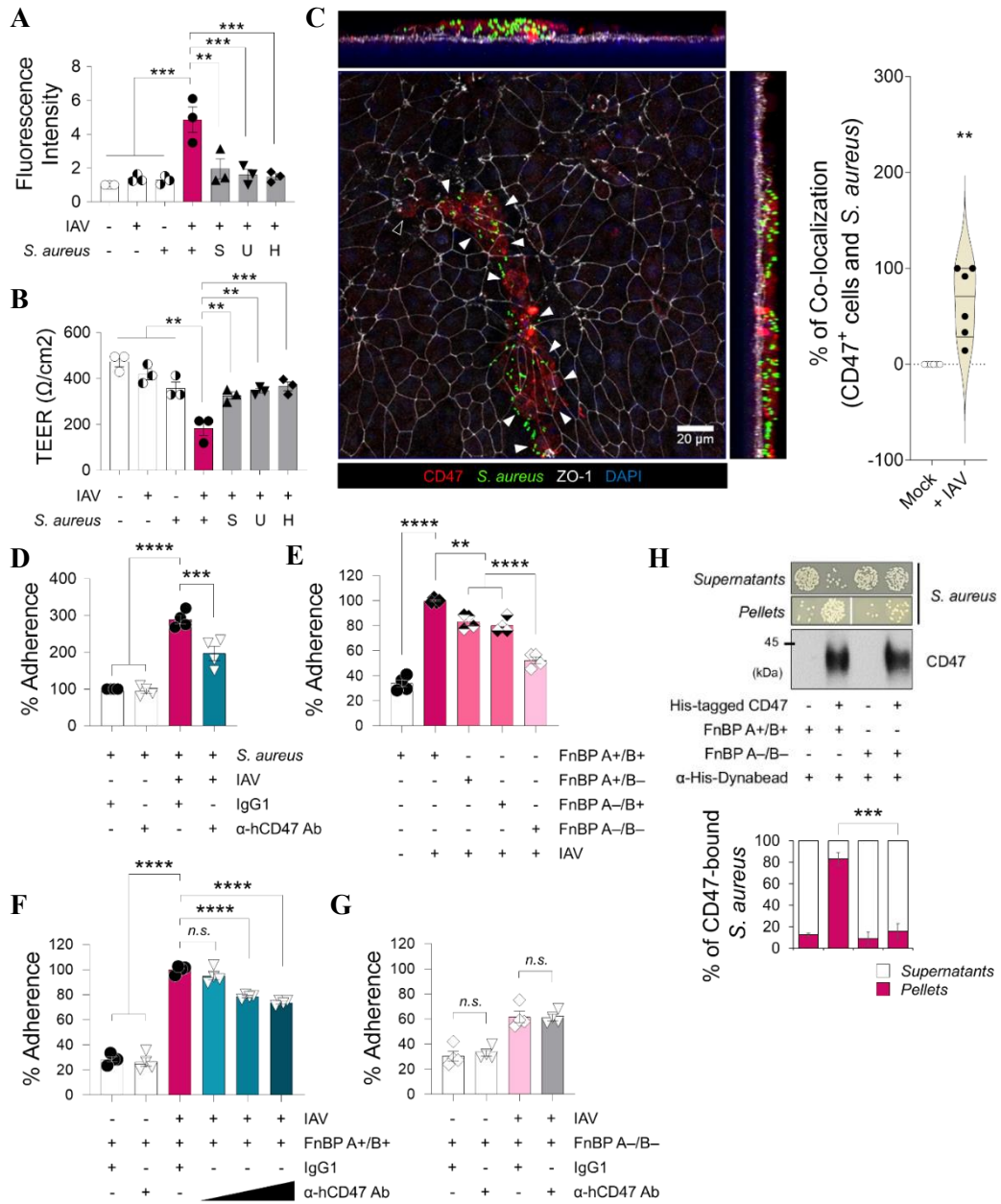


Figure 13. Epithelial CD47 and bacterial FnBP directly interacts. A, B Influenza virus-infected HBECs (+ IAV) infected with live *S. aureus* or *S. aureus*-derived samples (S,

supernatant of *S. aureus*-cultured media; *U*, UV-killed *S. aureus*; *H*, heat-killed *S. aureus*). Paracellular FITC-dextran permeability (**A**) and trans-epithelial electrical resistance (**B**) of 7 groups: *i*) mock, *ii*) virus only, *iii*) bacteria only, *iv*) super-infection, *v*) virus with *S*, *vi*) virus with *U*, and *vii*) virus with *H* ($n = 3$). **C** Whole mount image of CD47 (red) and *S. aureus* (green) in the influenza virus-infected HBECs at 1 dpi. An open arrow head indicates CD47⁺ cell without *S. aureus* and closed arrow heads indicate CD47⁺ cells with *S. aureus*. Co-localization of CD47⁺ cells and *S. aureus* are presented as violin plots (Mock, $n = 6$; + IAV, $n = 6$). **D-G** Bacterial adhesion assay. Colonization of *S. aureus* was assessed in HBECs inoculated with the virus (MOI 1) for 2 h before treatment with IgG1 control antibodies or α -hCD47 neutralizing antibodies (2 h), followed by *S. aureus* (MOI 3) infection for 3 h (IgG1 + *S. aureus*, $n = 4$; α -hCD47 Ab + *S. aureus*, $n = 4$; IgG1 + Super-infection, $n = 4$; α -hCD47 Ab + Super-infection, $n = 4$) (**D**). Adherence of *S. aureus* WT (FnBP A⁺/B⁺, $n = 4$) and three mutant strains (FnBP A⁺/B⁻, $n = 4$; FnBP A⁻/B⁺, $n = 4$; FnBP A⁻/B⁻, $n = 4$) was assessed in HBECs inoculated with the virus (MOI 1) for 2 h, followed by *S. aureus* (MOI 3) infection for 3 h (**E**). Colonization of *S. aureus* WT (FnBP A⁺/B⁺, $n = 4$) (**F**) and double deletion mutant (FnBP A⁻/B⁻, $n = 4$) (**G**) was assessed in HBECs inoculated with the virus (MOI 1) for 2 h before treatment with IgG1 control antibodies ($n = 4$) or α -hCD47 neutralizing antibodies (1, 5, and 10 μ g/mL for FnBP A⁺/B⁺, and 10 μ g/mL for FnBP A⁻/B⁻) for 2 h, followed by *S. aureus* (MOI 3) infection for 3 h ($n = 4$). **H** Pull-down assay using His-tagged hCD47 recombinant protein. Bacterial plating [*S. aureus* WT (FnBP A⁺/B⁺, $n = 3$ each in the absence or in the presence of His-tagged hCD47) and double deletion mutant (FnBP A⁻/B⁻, $n = 3$ each in the absence or in the presence of His-tagged hCD47)] and immunoblot analysis were performed using supernatants and pellets after separation with α -His-DynabeadsTM/DynaMagTM-2 system. The graphs present the percentage of colony numbers grown in the culture of the supernatants or the pellets. Results are shown as mean \pm SEM; ** $p < 0.01$; *** $p < 0.001$; **** $p < 0.0001$ using one-way ANOVA with Tukey's multiple comparisons test or Student's *t*-test. *n.s.*, not significant.

6. Foxj1^{Cre}-specific, but not LysM^{Cre}-specific, CD47 disruption protects mice from super-infection

Considering the increased expression of CD47 in the tracheal and lung epithelium (Figure 14E) and the decreased expression of ZO-1 in the lung lysates of C57BL/6 WT mice following infection with influenza virus (Figure 14F), I subsequently investigated the pathophysiological role of viral infection-induced CD47. As CD47 is ubiquitously expressed, understanding the contributions of specific CD47-expressing cell types during viral–bacterial super-infection is critical to gaining detailed mechanistic insights. Given that epithelial CD47 was exclusively induced in ciliated cells during viral infection (Figure 4E and Figure 6D), I generated mice with selective *CD47* loss in ciliated cells by creating *CD47* floxed mice (*CD47^{f/f}*), bred to constitutively express Cre under the control of the Foxj1 promoter (*Foxj1^{Cre}*)⁴⁸. Cre specificity was validated by crossing with tdTomato reporter mice (Figure 15A), in which *Foxj1^{tdTomato}*-expressing cells were co-stained with the ciliated cell-specific marker protein Ac- α -tubulin. Immunofluorescence confirmed the specific loss of *CD47* in ciliated cells of *CD47^{FoxJ1}* mice (Figure 15B). To ensure that CD47 inhibition during viral infection does not enhance innate immunity nor induce quicker virus clearance³¹, I also generated mice with selective loss of *CD47* in myeloid immune cells using *LysM^{Cre}* mice (*CD47^{LysM}*). Notably, *CD47^{FoxJ1}* and *CD47^{LysM}* mice did not exhibit differences in respiratory function under baseline conditions, compared with *CD47^{f/f}* mice (Figure 15C). To investigate the necessity of airway epithelial CD47 in the context of viral–bacterial super-infection, I established two in vivo mouse models of super-infection. As depicted in Figure 16A and 16L, I employed two different concentrations of virus and bacteria in both the CD47 gene deletion experiment (100 PFU of virus and 1 x 10⁸ CFU of bacteria) and the CD47 neutralizing experiment (10 PFU of virus and 5 x 10⁵ CFU of bacteria). Four groups of mice, including an uninfected group (Mock), a viral infection group, a bacterial infection group, and a super-infection group, were daily monitored for alterations in body weight and mortality over a 29-day period (Figure 16B and 16C). Remarkably, approximately 98% of the mice succumbed to the super-infection within 10

days, experiencing unrecoverable weight loss. To understand the underlying causes of this lethality, I assessed *i*) histological damage scores of lung sections, *ii*) total cell numbers in bronchoalveolar lavage (BAL) fluids, *iii*) bacterial burden in the lung and the spleen, *iv*) concentrations of total protein, and *v*) levels of pro-inflammatory cytokines (TNF- α and IL-6) in BAL fluids at 24 hours following bacterial infection. In all these parameters, the super-infection group exhibited significantly increased values compared to the mock, viral infection, and bacterial infection groups (Figure 16D-K). Subsequently, I investigated whether the presence of airway epithelial CD47 or myeloid CD47 is essential for viral-bacterial super-infection. I conducted experiments using 7–8-weeks-old mice weighing between 18–21 grams with specific genetic modifications: FoxJ1-Cre;floxed ($Cd47^{FoxJ1}$), LysM-Cre;floxed ($Cd47^{LysM}$), and control floxed ($Cd47^{fl/fl}$) mice. These mice were infected with 100 PFU of influenza virus on day 0, followed by an infection of 1×10^8 CFU of *S. aureus* on day 7. Body weight loss and survival rates were monitored for 29 days. Notably, $CD47^{FoxJ1}$ mice exhibited a recovery in body weight loss and improved survival rates compared to $CD47^{fl/fl}$ mice (Figure 17A and 17B), while $CD47^{LysM}$ mice did not show the same improvements (Figure 17K and 17L). Moreover, signs of pneumonia were significantly alleviated in $CD47^{FoxJ1}$ mice (Figure 17C-J) but not in $CD47^{LysM}$ mice (Figure 17M-T) when compared to $CD47^{fl/fl}$ mice. This improvement was evident through several measures: *i*) a reduced histological lung injury score (Figure 17C), *ii*) decreased total cell numbers in BAL fluids (BALF) (Figure 17D), *iii*) diminished bacterial adherence and invasion in the lung (Figure 17E and 17F) and bacterial burden in the spleen (Figure 17G), *iv*) reduced total protein levels (Figure 17H), and *v*) decreased levels of TNF- α and IL-6 in BALF 24 h after bacterial infection (Figure 17I and 17J). These findings underscore the protective effect of inhibiting CD47 specifically in ciliated cells rather than myeloid cells against viral-bacterial super-infection.

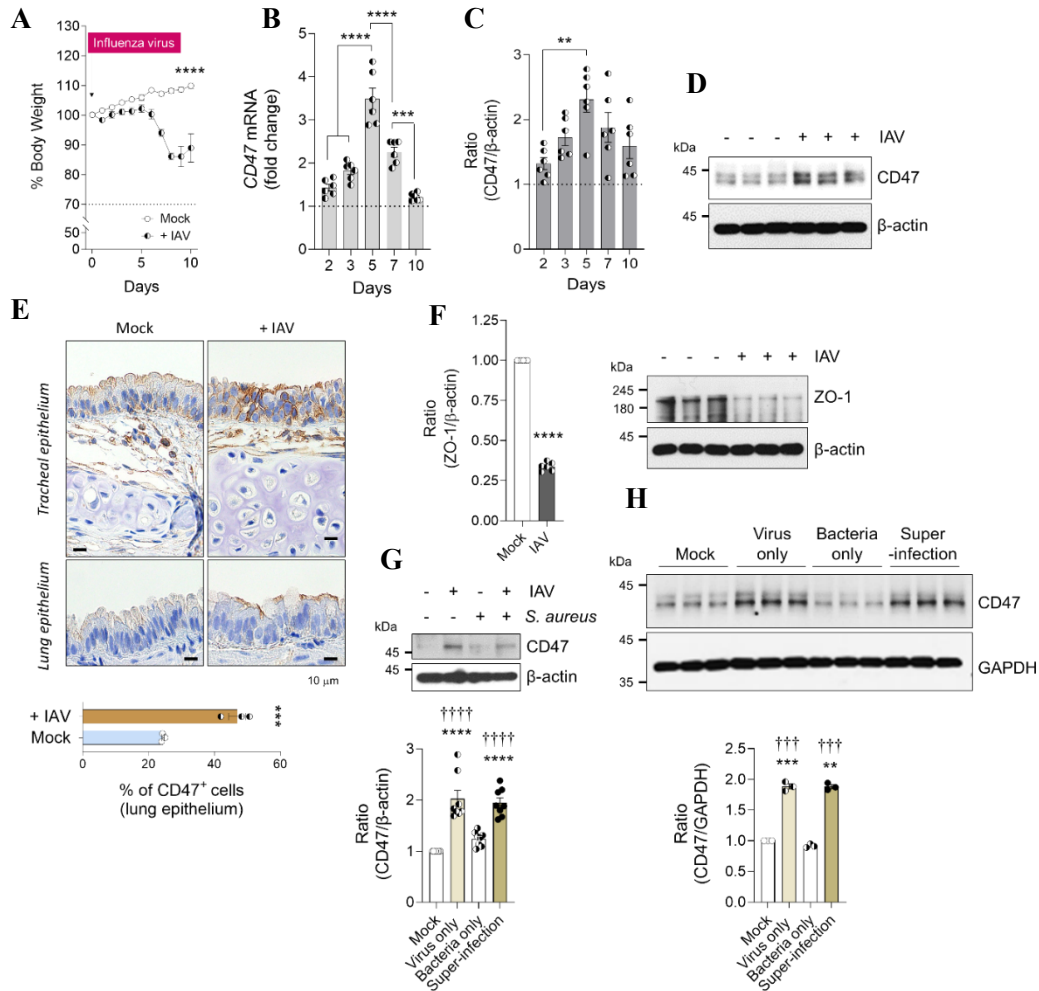


Figure 14. Induction of CD47 upon viral infection. A-F 6–8-weeks-old (18–21 g of body weight) C57BL/6 WT mice were infected with influenza virus (100 PFU). Body weight loss was monitored in two groups of mice for 10 days; non-infected (*Mock*) and influenza virus-infected (+ *IAV*) (A). The dotted line indicates the body weight exclusion cut-off. Changes in *CD47* mRNAs ($n = 6$) (B) and *CD47* proteins ($n = 6$) (C) were analyzed at 2, 3, 5, 7 and 10 dpi. Representative immunoblots of *CD47* at 5 dpi (D). Cross section of tracheal epithelium (*upper panels*) and lung epithelium (*lower panels*) at 7 dpi were stained with antibodies against *CD47* and visualized via 3, 3'-diaminobenzidine

tetrahydrochloride (DAB) staining (E). The slides were counterstained with hematoxylin. Percentages of CD47-positive cells were presented as bar graphs ($n = 3$). Changes in ZO-1 proteins were analyzed at 5 dpi. Normalized ZO-1 protein levels are presented as bar graphs ($n = 6$) (F). G-H Changes in CD47 proteins were analyzed in HBECs ($n = 6$) (G) or four groups of control floxed ($CD47^{fl/fl}$) mice (whole lung lysates, $n = 3$) (H); non-infected (*Mock*), influenza virus-infected (*Virus only*), *S. aureus*-infected (*Bacteria only*), and viral-bacterial co-infected mice (*Super-infection*). Normalized CD47 protein levels are presented as bar graphs. Results are the mean \pm SEM; ** $p < 0.01$; *** $p < 0.001$; **** $p < 0.0001$ vs. *Mock* (††† $p < 0.001$; †††† $p < 0.0001$ vs. *Bacteria only*) using one-way ANOVA with Tukey's multiple comparisons test or two-way ANOVA with Tukey's multiple comparisons test (% Body weight).

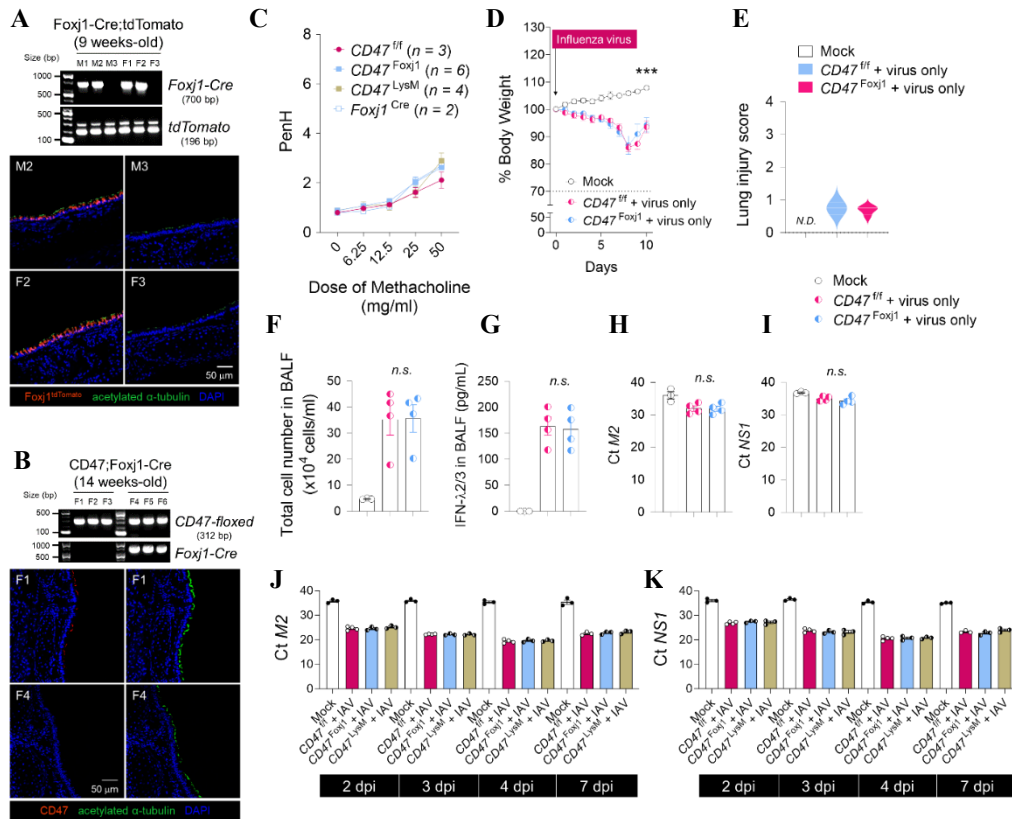


Figure 15. Characterization of tissue-specific CD47 deletion mice. **A** Specificity of *Foxj1*-Cre was validated using *Foxj1*-Cre;tdTomato mice (trachea). PCR amplification of mice genomic DNA using the specific primers for *Foxj1*-Cre and *tdTomato* (**upper panels**). *Foxj1*^{tdTomato}-expressing cells (red) were co-stained with ciliated cell-specific marker protein Ac- α -tubulin (green) (**lower panels**). **B** *Foxj1*^{Cre}-specific CD47 deletion was determined in the lower airway epithelium (trachea). PCR amplification of mice genomic DNA using the specific primers for *CD47*-floxed cassette and *Foxj1*-Cre (**upper panels**). CD47-expressing cells (red) and ciliated cell-specific marker protein Ac- α -tubulin (green) are shown on the same slide separately (**lower panels**). **C** Airway hyper-responsiveness (AHR) is presented as Penh in response to methacholine. **D-I** 6–8-weeks-old (18–21 grams of body weight) *Foxj1*-Cre;floxed (*Cd47*^{Foxj1}) mice and control floxed (*Cd47*^{fl/fl}) mice were

infected with influenza virus (100 PFU). Body weight loss was monitored in two groups of mice for 10 days ($n \geq 3$) (**D**). Lung injury scores are presented as violin plots ($n \geq 3$) (**E**). Total cell number in BAL fluids (BALF) (**F**) and levels of type III interferons (IFN- λ 2/3) were measured at 10 dpi ($n \geq 3$) (**G**). **H-I** Mouse lungs were harvested at 10 dpi for qPCR analysis to evaluate the transcriptional level of viral *M2* (**H**) and *NSI* (**I**) genes in virus-infected *CD47^{f/f}* and *CD47^{Foxj1}* compared with Mock ($n \geq 3$). **J-K** Mouse lungs were harvested at 2, 3, 4 and 7 dpi for qPCR analysis to evaluate the transcriptional level of viral *M2* (**J**) and *NSI* (**K**) genes in virus-infected *CD47^{f/f}*, *CD47^{Foxj1}*, and *CD47^{LysM}* mice compared with Mock ($n \geq 3$). Results are the mean \pm SEM; *p* values were analyzed using one-way ANOVA with Tukey's multiple comparisons test. *M*, male; *F*, female; bp, base pair; *N.D.*, not detected; *n.s.*, not significant.

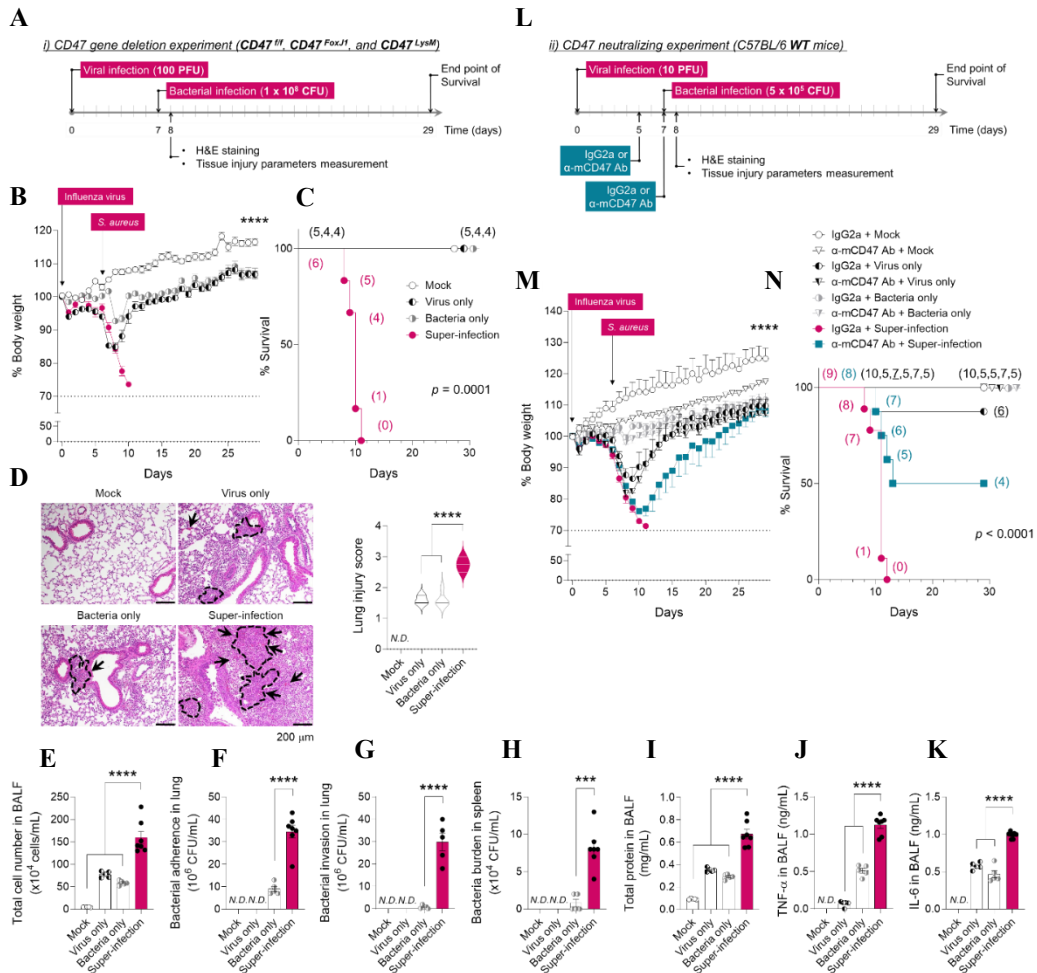


Figure 16. Two in-vivo models of super-infection used in this study. A-K For CD47 gene deletion experiment (A), 7–8-weeks-old (18–21 grams of body weight) control floxed ($Cd47^{fl/fl}$) mice were infected with 100 PFU of influenza virus on day 0 and with 1×10^8 CFU of *S. aureus* on day 7. Body weight loss (B) and survival rates (C) were monitored in four groups of mice for 29 days; non-infected (*Mock*, $n = 5$), influenza virus-infected (*Virus only*, $n = 4$), *S. aureus*-infected (*Bacteria only*, $n = 4$), and viral bacterial co-infected mice (*Super-infection*, $n = 6$). Representative hematoxylin and eosin (H&E) staining of lung

sections in four groups (**D**). The dotted lines indicate lymphocytic infiltration and arrows indicate alveolar hemorrhage. Lung injury scores are presented as violin plots. Tissue injury parameters were measured at 24 h after bacterial infection: total cell number in BAL fluids (**E**), bacterial adherence (**F**) and invasion (**G**) in the lung, and bacterial burden in the spleen (**H**) total protein concentrations in BAL fluids (**I**), and inflammatory cytokines TNF- α (**J**) and IL-6 (**K**) in BAL fluid ($n \geq 5$). **L-N** For CD47 neutralizing experiment (**L**), 7–8-week-old (18–21 grams of body weight) C57BL/6 WT mice were infected with 10 PFU of influenza virus on day 0 and with 5×10^5 CFU of *S. aureus* on day 7. Before bacterial infection, mice were intranasally treated twice with IgG2a control antibodies (2A3) or α -mCD47 neutralizing antibodies (MIAP301) at 5 and 7 dpi. Body weight loss (**M**) and survival rate (**N**) were monitored in eight groups of mice for 29 days; *IgG2a + Mock* ($n = 10$), *α -mCD47 Ab + Mock* ($n = 5$), *IgG2a + Virus only* ($n = 8$), *α -mCD47 Ab + Virus only* ($n = 5$), *IgG2a + Bacteria only* ($n = 8$), *α -mCD47 Ab + Bacteria only* ($n = 5$), *IgG2a + Super-infection* ($n = 9$), and *α -mCD47 Ab + Super-infection* ($n = 8$). The dotted line indicates the body weight exclusion cut-off. A mantel cox survival analysis was used to compare the survival rates between groups. The numbers in parenthesis represent the count of surviving mice. Results are presented as the mean \pm SEM; *** $p < 0.001$; **** $p < 0.0001$ using one-way ANOVA with Tukey's multiple comparisons test or two-way ANOVA with Tukey's multiple comparisons test (% Body weight). *N.D.*, not detected.

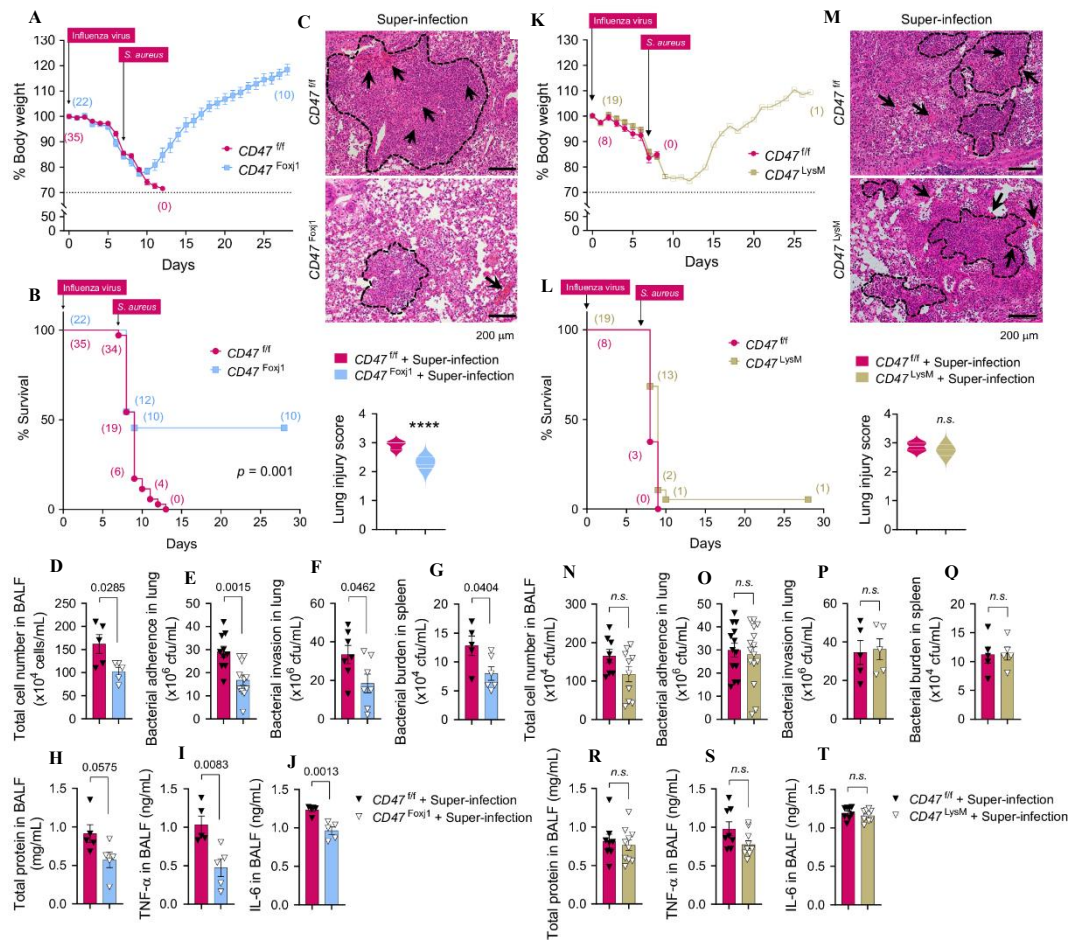


Figure 17. Foxj1^{Cre}-Specific, but not LysM^{Cre}-Specific, CD47 disruption protects mice from super-infection. 6–8-weeks-old (18–21 g of body weight) *FoxJ1*-Cre;floxed (*CD47^{Foxj1}*), *LysM*-Cre;floxed (*CD47^{LysM}*), and control floxed (*CD47^{fl/fl}*) mice were infected with 100 PFU of influenza virus on day 0, and 1×10^8 CFU of *S. aureus* on day 7. **A, B, K, L** Body weight loss (**A, K**) and survival rates (**B, L**) were monitored for 29 days. The dotted line indicates the body weight exclusion cut-off. A mantel cox survival analysis was used to compare the survival rates between groups. The numbers in parenthesis represent the count of surviving mice. **C, M** Representative hematoxylin and eosin (H&E)

staining of lung sections. The dotted lines indicate lymphocytic infiltration and arrows indicate alveolar hemorrhage. Lung injury scores are presented as violin plots in $CD47^{Foxj1}$ mice ($CD47^{fl/fl}$, $n = 8$; $CD47^{Foxj1}$, $n = 5$) (C) and $CD47^{LysM}$ mice ($CD47^{fl/fl}$, $n = 8$; $CD47^{LysM}$, $n = 8$) (M). D–J, N–T Tissue injury parameters were measured at 24 h after bacterial infection; total cell number in BAL fluids (BALF) of $CD47^{Foxj1}$ mice ($CD47^{fl/fl}$, $n = 5$; $CD47^{Foxj1}$, $n = 5$) (D) and $CD47^{LysM}$ mice ($CD47^{fl/fl}$, $n = 8$; $CD47^{LysM}$, $n = 10$) (N); bacterial adherence in the lung of $CD47^{Foxj1}$ mice ($CD47^{fl/fl}$, $n = 10$; $CD47^{Foxj1}$, $n = 11$) (E) and $CD47^{LysM}$ mice ($CD47^{fl/fl}$, $n = 13$; $CD47^{LysM}$, $n = 15$) (O); bacterial invasion in the lung of $CD47^{Foxj1}$ mice ($CD47^{fl/fl}$, $n = 7$; $CD47^{Foxj1}$, $n = 7$) (F) and $CD47^{LysM}$ mice ($CD47^{fl/fl}$, $n = 5$; $CD47^{LysM}$, $n = 5$) (P); and bacterial burden in the spleen of $CD47^{Foxj1}$ mice ($CD47^{fl/fl}$, $n = 5$; $CD47^{Foxj1}$, $n = 6$) (G) and $CD47^{LysM}$ mice ($CD47^{fl/fl}$, $n = 5$; $CD47^{LysM}$, $n = 5$) (Q); total protein concentrations in BALF of $CD47^{Foxj1}$ mice ($CD47^{fl/fl}$, $n = 5$; $CD47^{Foxj1}$, $n = 5$) (H) and $CD47^{LysM}$ mice ($CD47^{fl/fl}$, $n = 8$; $CD47^{LysM}$, $n = 10$) (R); and inflammatory cytokines TNF- α in BALF of $CD47^{Foxj1}$ mice ($CD47^{fl/fl}$, $n = 5$; $CD47^{Foxj1}$, $n = 5$) (I) and $CD47^{LysM}$ mice ($CD47^{fl/fl}$, $n = 8$; $CD47^{LysM}$, $n = 10$) (S), and IL-6 in BALF of $CD47^{Foxj1}$ mice ($CD47^{fl/fl}$, $n = 5$; $CD47^{Foxj1}$, $n = 5$) (J) and $CD47^{LysM}$ mice ($CD47^{fl/fl}$, $n = 8$; $CD47^{LysM}$, $n = 10$) (T). Data are presented as mean values \pm SEM. Significance was determined by unpaired two-tailed Student's t test.

7. Antibody-mediated CD47 neutralization protects mice from super-infection

Next, I examined the efficacy of antibody-mediated CD47 blockade in inhibiting viral-bacterial super-infection. C57BL/6 WT mice pre-treated with α -mCD47 neutralizing antibodies exhibited a recovery in body weight loss (Figure 18A) and improved survival rates (Figure 18B) compared to C57BL/6 WT mice pre-treated with IgG2a control antibodies. Additionally, signs of pneumonia were significantly alleviated in α -mCD47-treated mice compared to IgG2a-treated mice, as evidenced by a decrease in histological lung injury score (Figure 18C), a reduction in total cell number in BALF (Figure 18D), a decrease in bacterial adherence and invasion in the lung (Figure 18E and 18F) and bacterial burden in the spleen (Figure 18F), a decline in total protein levels (Figure 18G), and a decrease in TNF- α and IL-6 in BALF (Figure 18H and 18I). These findings indicate that therapeutically inhibiting CD47 protects mice from viral-bacterial super-infection.

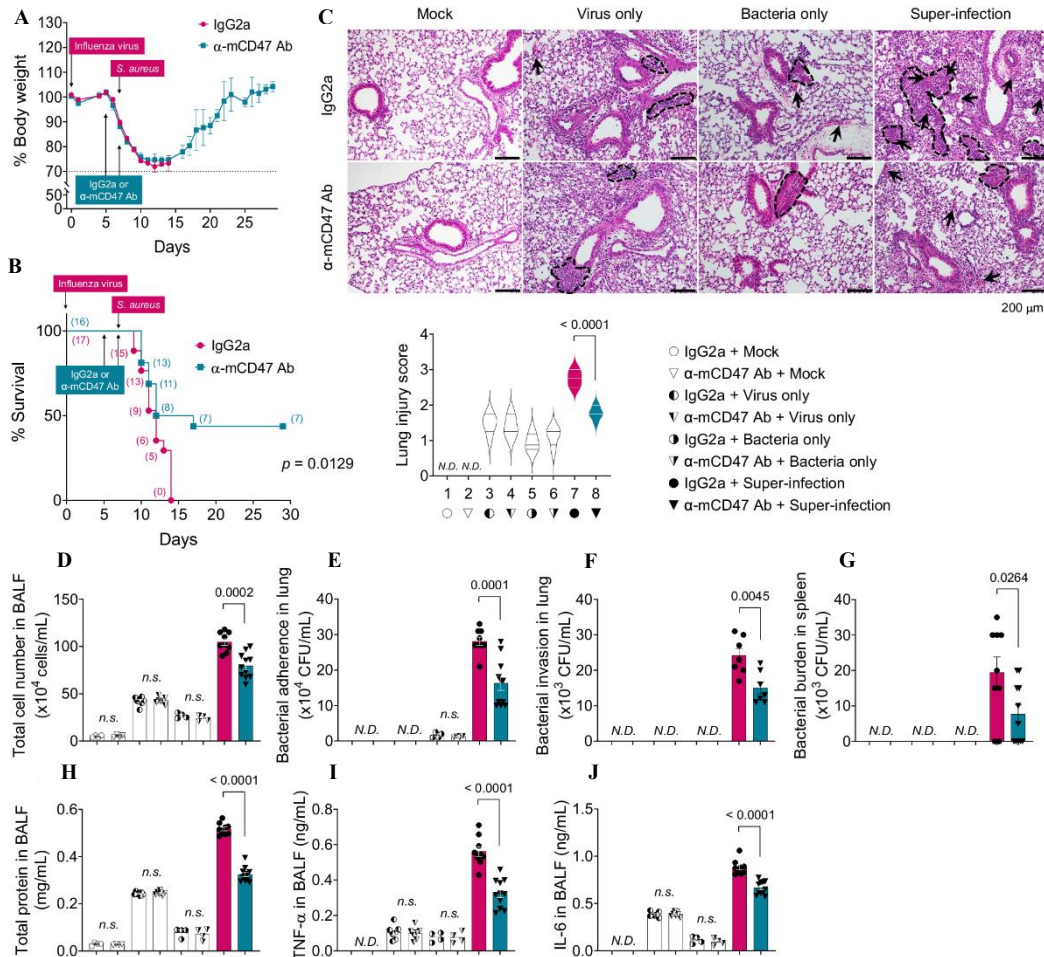


Figure 18. CD47 neutralization enhances protection against super-infection. For neutralization test, 6–8-weeks-old (18–21 g of body weight) C57BL/6 WT mice were infected with 10 PFU of influenza virus on day 0 and 5×10^5 CFU of *S. aureus* on day 7. Before bacterial infection, mice were intranasally treated twice at day 5 and 7 with IgG2a control antibodies (2A3, $n = 17$) or α -mCD47 neutralizing antibodies (MIAP301, $n = 16$). **A, B** Body weight loss (**A**) and survival rates (**B**) were monitored for 29 days. The dotted line indicates the body weight exclusion cut-off. A mantel cox survival analysis was used to compare the survival rates between groups. The numbers in parenthesis are numbers of

survived mice. **C** Representative hematoxylin and eosin (H&E) staining of lung sections (*IgG2a + Mock*, $n = 4$; *α -mCD47 Ab + Mock*, $n = 4$; *IgG2a + Virus only*, $n = 7$; *α -mCD47 Ab + Virus only*, $n = 7$; *IgG2a + Bacteria only*, $n = 4$; *α -mCD47 Ab + Bacteria only*, $n = 4$; *IgG2a + Super-infection*, $n = 9$; *α -mCD47 Ab + Super-infection*, $n = 11$). The dotted lines indicate lymphocytic infiltration and arrows indicate alveolar hemorrhage. Lung injury scores are presented as violin plots. **D–J** Tissue injury parameters were measured at 24 h after bacterial infection (*IgG2a + Mock*, $n = 4$; *α -mCD47 Ab + Mock*, $n = 4$; *IgG2a + Virus only*, $n = 7$; *α -mCD47 Ab + Virus only*, $n = 7$; *IgG2a + Bacteria only*, $n = 4$; *α -mCD47 Ab + Bacteria only*, $n = 4$; *IgG2a + Super-infection*, $n = 7-9$; *α -mCD47 Ab + Super-infection*, $n = 7-11$); total cell number in BAL fluids (BALF) (**D**), bacterial adherence (**E**) and invasion (**F**) in the lung, and the bacterial burden in the spleen (**G**), total protein concentrations (**H**) in BALF, and inflammatory cytokines TNF- α (**I**) and IL-6 (**J**) in BALF. Data are presented as mean values \pm SEM. Significance was determined by unpaired two-tailed *t* test. n.s. not significant. N.D. not determined.

8. Interaction between epithelial CD47 and bacterial FnBP is essential to cause super-infection

To fully confirm the interaction between FnBP and CD47 *in vivo*, I infected both $CD47^{fl/fl}$ and $CD47^{FoxJ1}$ mice with two *S. aureus* strains, FnBP A+/B+ and FnBP A-/B-, to verify whether the observed phenotype aligns with my expected model⁴⁹. As expected, FnBP A-/B- exhibited reduced pathogenicity when infecting $CD47^{fl/fl}$ mice, similar to the effect of FnBP A+/B+ in $CD47^{FoxJ1}$ mice, while there was no observable effect when either FnBP A+/B+ or FnBP A-/B- infected $CD47^{FoxJ1}$ mice (Figure 19A-J). Taken together, my results demonstrate that both airway epithelial CD47 and *S. aureus* FnBP are essential for the development of viral-bacterial super-infection (Figure 20).

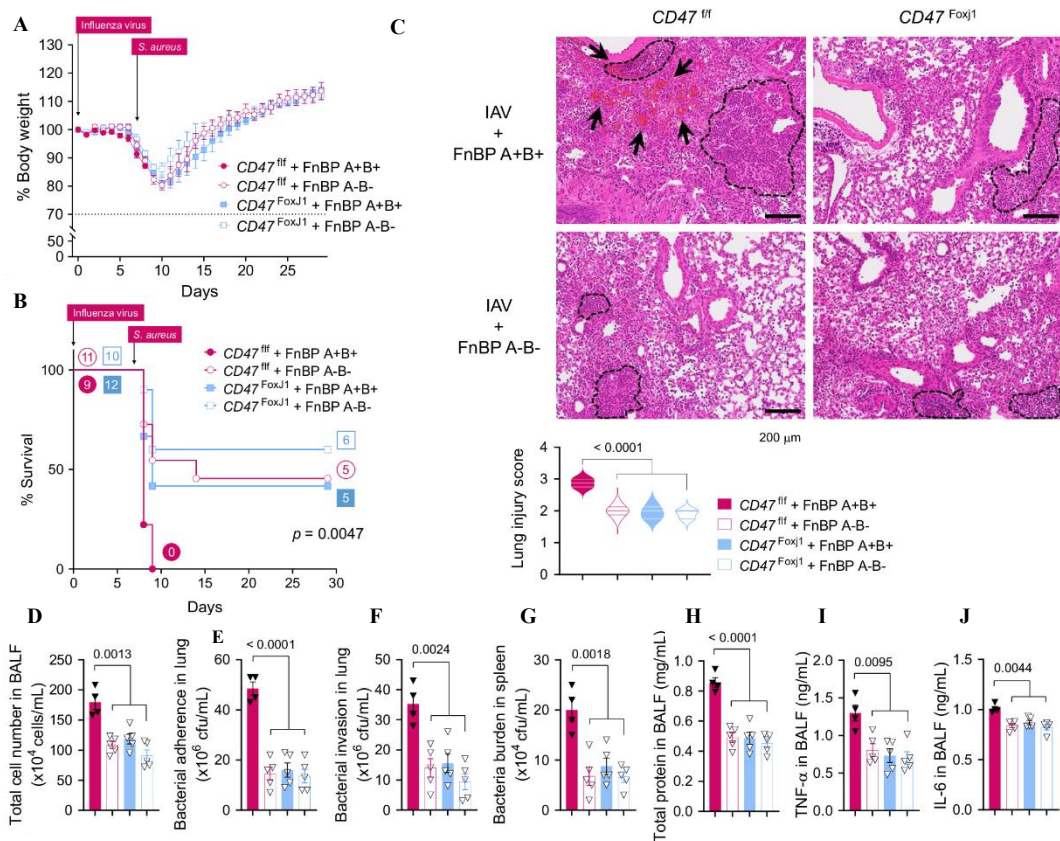


Figure 19. Interaction between epithelial CD47 and bacterial FnBP is essential to cause super-infection. 6–8-weeks-old (18–21 g of body weight) *FoxJ1-Cre*; floxed ($Cd47^{Foxj1}$) and control floxed ($Cd47^{fl/fl}$) mice were infected with 100 PFU of influenza virus on day 0, and 1×10^8 CFU of *S. aureus* WT (FnBP A+/B+) and double deletion mutant (FnBP A-/B-) on day 7 ($Cd47^{fl/fl} + FnBP A+/B+$, $n = 9$; $Cd47^{fl/fl} + FnBP A-/B-$, $n = 11$; $Cd47^{Foxj1} + FnBP A+/B+$, $n = 12$; $Cd47^{Foxj1} + FnBP A-/B-$, $n = 10$). Body weight loss (A) and survival rates (B) were monitored for 29 days. The dotted line indicates the body weight exclusion cut-off. A mantel cox survival analysis was used to compare the survival rates between groups. The numbers within circles or squares represent the count of surviving mice. Representative hematoxylin and eosin (H&E) staining of lung sections (C). Lung

injury scores are presented as violin plots ($Cd47^{fl/fl} + \text{FnBP A+/B+}$, $n = 4$; $Cd47^{fl/fl} + \text{FnBP A-}/\text{B-}$, $n = 5$; $Cd47^{\text{Foxj1}} + \text{FnBP A+/B+}$, $n = 5$; $Cd47^{\text{Foxj1}} + \text{FnBP A-}/\text{B-}$, $n = 5$). Tissue injury parameters were measured at 24 h after bacterial infection ($Cd47^{fl/fl} + \text{FnBP A+/B+}$, $n = 4$; $Cd47^{fl/fl} + \text{FnBP A-}/\text{B-}$, $n = 5$; $Cd47^{\text{Foxj1}} + \text{FnBP A+/B+}$, $n = 5$; $Cd47^{\text{Foxj1}} + \text{FnBP A-}/\text{B-}$, $n = 5$); total cell number in BAL fluids (BALF) (**D**), bacterial adherence (**E**) and invasion (**F**) in the lung, and bacterial burden in the spleen (**G**), total protein concentrations in BALF (**H**), and inflammatory cytokines TNF- α (**I**) and IL-6 (**J**) in BALF. Data are presented as mean values \pm SEM. Significance was determined by one-way ANOVA with Tukey's multiple comparisons test.

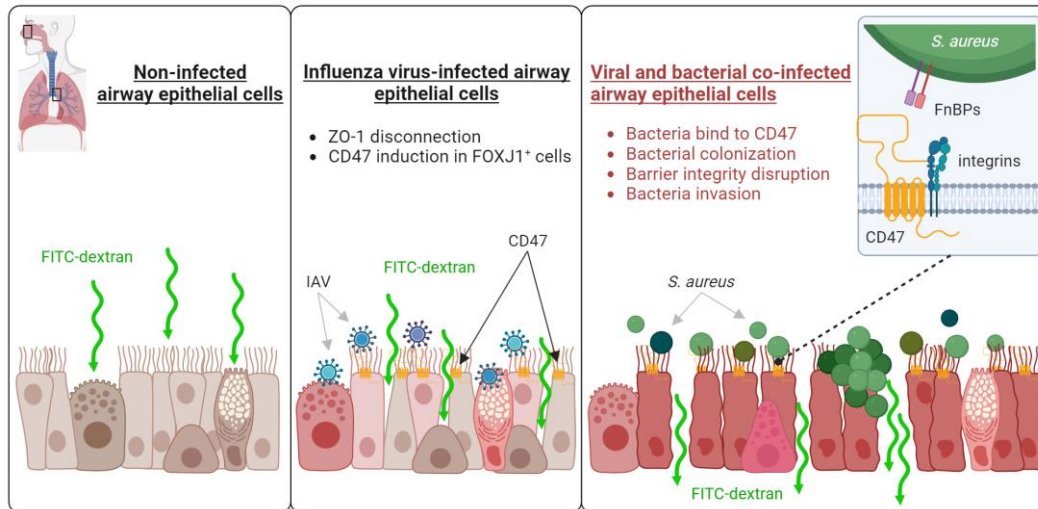


Figure 20. Proposed model of viral infection-induced CD47-mediated bacterial secondary infection. Schematic illustration delineating the structure of the airway epithelium. Airway epithelium is mainly composed of ciliated cells, goblet cells, and basal cells. Non-infected airway epithelial cells maintain barrier integrity, which consists of junctional complexes (**left**). Influenza virus infection induces and exposes on the apical surface of FoxJ1⁺ cells. Influenza virus-infected airway epithelial cells specifically affected ZO-1 without causing significant disruption of barrier integrity (**middle**). Direct interactions between virus-induced CD47 and Fn-binding protein (FnBP) of *S. aureus* in viral and bacterial co-infected airway epithelial cells causes bacterial colonization and significant disruption of barrier integrity (**right**).

Table 1. List of primers used in this study.

Gene	Forward primer sequence 5' -> 3'	Reverse primer sequence 5' -> 3'
Human <i>CD47</i>	TCGGTCCTGCCTGTAACG	TACCAGGGGCCACATCTC
Human <i>ZO-1</i>	TGGTGTCTACCTAATCAACTCA	CGCCAGCTACAAATATTCCAACA
Human <i>ICAM-1</i>	CCTTCCTCACCGTGTACTGG	AGCGTAGGGTAAGGTTCTTGC
Human <i>CEACAM5</i>	AGGCCAATAACTCAGCCAGT	GGGTTTGAGATTGTTGCTGG
Human <i>PAFR</i>	AACCAGGGCAACTGGATACTC	AAGGCCACAGAGCAGTAGGT
Human <i>Integrin α3</i>	AAGGGACCTTCAGGTGCA	TGTAGCCGGTGATTACCAT
Human <i>Integrin β1</i>	GAAGGGTTGCCCTCCAGA	GCTTGAGCTTCTCTGTCTGTT
Human <i>Interferon β1</i>	ATTCTAACTGCAACCTTTTCG	GTTGTAGCTCATGGAAAGAG
Human <i>Interferon λ1</i>	GACTTTGGTGCTAGGCTTGG	AGATTTGAACCTGCCAATGTG
Human <i>Interferon λ2/3</i>	GCCAAAGATGCCTTAGAAGAG	CAGAACCTTCAGCGTCAGG
Human <i>Mx1</i>	AGAGAAGGTGAGAAGCTGATCC	TTCTTCCAGCTCCTTCTCTCTG
Human <i>Oas1</i>	GCTCCTACCCTGTGTGTGTGT	TGGTGAGAGGACTGAGGAAGA
Influenza virus <i>M2</i>	AAGACCAATCCTGTCACTCTGA	CAAAGCGTCTACGCTGCAGTCC
Influenza virus <i>NS1</i>	AGCAAAAAGCAGGGTGACA AAGACA	TCGGTGAAAGCCCTTA
Mouse <i>CD47</i>	AGGATGGCGTGAGGGAGAGC	CTCTTATTCTGTATGGCTG
<i>Δ fnbB</i>	CGCAGTGTTGAGATACCATGAG	GGAAAGTGGGAGTTCAGCTACTG
<i>Δ sdrE</i>	GCTTTGCAGTTGCAACAACCAGC	CTTTGAGGCAATTGTTGATCAGAG
<i>Δ clfA</i>	GCAATCAAATCGTACGTTGTCTG	GTAGTAGCTTACCAGTTACCGG
<i>Δ isdB</i>	GGTTGTGCGAATTCATTAATGTG	TGTCAAATGGCGAAGCACAAGC
<i>Δ sasG</i>	CTCTGCGTTATGAGTGACTGACG	GTGTTATATTCCATTGTGCAACTCC
<i>GAPDH</i>	CAATGACCCCTTCATTGACC	GACAAGCTTCCCCTTCTCAG
<i>Ppia</i>	CGCTTGCTGCAGCCATGGTC	CAGCTCGAAGGAGACGCGGC
18s	GCTTAATTTGACTCAACACGGGA	AGCTATCAATCTGTCAATCCTGTG
<i>GAPDH</i>	CAATGACCCCTTCATTGACC	GACAAGCTTCCCCTTCTCAG
<i>tdTomato</i> Wildtype	AAGGGAGCTGCAGTGGAGTA	CCGAAAATCTGTGGGAAGTC
<i>tdTomato</i> Mutant	CTGTTCTGTACGGCATGG	GGCATTAAAGCAGCGTATCC
<i>LysM-Cre</i> Wildtype	CTTGGGCTGCCAGAATTTCTC	TTACAGTCGGCCAGGCTGAC
<i>LysM-Cre</i> Mutant	CTTGGGCTGCCAGAATTTCTC	CCCAGAAATGCCAGATTACG
<i>Foxj1-Cre</i>	GCCTGCATTACCGGTGATGCAACGA	GTGGCAGATGGCGCGCAACACCATT
<i>CD47</i> -floxed	TCTACACTAACTCAGCTGGCCTGG	CTGTCTCTGTGCTCTCTGGCTAAGG

IV. DISCUSSION

The upregulation of CD47 in response to viral infections other than influenza has been documented in previous studies⁵⁰⁻⁵². For instance, human respiratory syncytial virus (RSV) and human parainfluenza virus 3 (HPIV3) infections have been shown to increase CD47 levels⁵⁰. Additionally, CD47 expression is elevated in cells infected with SARS-CoV-2⁵². McLaughlin et al. conducted an analysis of publicly available proteomics⁵³ and transcriptomics⁵⁴ data, revealing increased CD47 expression in SARS-CoV-2-infected HBECs and Caco2 cells. However, the specific role of viral infection-induced CD47 in the context of pathogenic bacterial infection remains unclear. In this study, I provide evidence that: *i*) Influenza viral infection induces the upregulation of airway epithelial CD47, particularly in ciliated cells, accompanied by barrier integrity disruption. *ii*) FnBP, a member of the microbial surface components recognizing adhesive matrix molecules (MSCRAMM) family, plays a crucial role in the attachment of pneumonia-causing pathogenic bacteria such as *S. aureus*. *iii*) CD47 neutralizing antibodies protect mice from secondary bacterial infection by blocking the direct interaction between CD47 and FnBP. These findings shed light on the complex interplay between viral infections and bacterial pathogens, particularly in the context of CD47 upregulation and its impact on host defenses.

The upper and lower airways are lined by a pseudostratified epithelium composed of ciliated, goblet, and basal cells⁴². In human tissues, influenza viruses primarily bind to ciliated cells, whereas in differentiated airway epithelial cell cultures, they infect non-ciliated cells and, to a lesser extent, ciliated cells⁵⁵. Recent studies have indicated that SARS-CoV-2 also exhibit a preference for targeting ciliated cells and interferes with mucociliary clearance⁵⁶. It's important to note that while CD47 induction by viral infection is specific to ciliated cells (Figure 4E and Figure 6D), not all ciliated cells were infected (Figure 5B). Given that virus-induced IFNs are secreted and signal on neighboring cells⁵⁷, the observed expression pattern can be explained. Although it could be speculated that virus-infected cells experience a more suppressed IFN response due to viral mechanisms

inhibiting IFN signals, whereas uninfected cells exhibit a full response to IFN, resulting in the upregulation of CD47, the precise mechanism by which neighboring infected cells induce CD47 in ciliated cells remains unclear at this stage. Pathogenic bacteria possess a multitude of virulence factors that enable them to bind to host receptors or extracellular matrix (ECM) components^{4,45,46}. While my in-depth investigation primarily focused on the membrane proteins of *S. aureus* as a microbial component responsible for interacting with epithelial CD47, additional research is necessary to uncover the specific surface proteins binding to CD47 in other pneumonia-causing pathogenic bacteria, such as *S. pneumoniae*, *Haemophilus influenzae*, and *Streptococcus hemolyticus*. The FnBP-Fn- $\alpha 5\beta 1$ integrin pathway is recognized as the primary adhesion and internalization process; however, it is important to note that additional factors have been shown to influence the efficiency of this process. For example, Dziewanowska et al. reported that the direct interaction between FnBPs and Hsp60 maximizes the internalization efficiency in epithelial cells⁵⁸. Further investigation is required to determine whether CD47 acts as a co-receptor, enhancing the binding of FnBP-Fn to $\alpha 5\beta 1$ integrin.

I assessed CD47 mRNA levels (Figure 14B) and protein levels (Figure 14C and 14D) at multiple time points, including 2, 3, 5, 7, and 10 dpi. Notably, both mRNA and protein levels exhibited a gradual increase, reaching their peak at 5 dpi, followed by a subsequent decrease. Intriguingly, in contrast to this observation, *S. aureus* single infection failed to induce CD47 expression in both *in vitro* and *in vivo* settings. Furthermore, no synergistic effect was observed with viral infection, as evidenced in Figure 14G and 14H. This time course data provides valuable insights into how CD47 expression correlates with the window of enhanced susceptibility to secondary infection, which is typically observed between days 5-10 post-infection with influenza virus^{59,60}. Two potential explanations may account for the expression of CD47 on the surface of host epithelial cells in response to viral infection. In the context of viral propagation, viruses may employ CD47 surface expression as a strategy to evade immune cells presenting "don't-eat-me" signals, similar to their actions in infected hematopoietic cells^{30,31}. Second, in order to support their

systemic proliferation, viruses could induce epithelial cells to express binding sites for bacteria. In the context of host signaling, it is conceivable that virus-infected epithelial cells might stimulate CD47 expression via the NF- κ B signaling pathway, as has been reported for ICAM-1^{19,23}.

Due to the methodological challenges inherent in my primary epithelial cell ALI culture setup, I was unable to distinctly differentiate between bacterial adherence and invasion *in vitro*. Instead, I utilized a super-infection mouse model to evaluate both the adherence of *S. aureus* and its invasion into the lung tissue⁶¹, as well as bacterial CFU in the spleen as an indicator of systemic bacterial dissemination⁶². In order to establish an *in vivo* correlation with the observed loss of the epithelial barrier function in my *in vitro* super-infection model (Figure 9 and Figure 10), I validated the downregulation of ZO-1 in the lung following viral infection (Figure 14F) and the increases in *S. aureus* invasion in the lung (Figure 16G and Figure 18F) and bacteremia during super-infection (Figure 16H and Figure 18G). My findings demonstrated that the absence of CD47 in ciliated cells (Figure 17F) or the absence of FnBP in *S. aureus* (Figure 19F) indeed provided protection against *S. aureus* invasion. Notably, this protective effect was not observed in myeloid cell-specific knockout mice (Figure 17P and 17Q). Additionally, the use of anti-CD47 neutralizing antibody treatment proved effective in preventing bacterial invasion (Figure 18F). Nonetheless, I have not yet been able to elucidate the precise mechanisms by which the accumulated bacteria breach the barrier more effectively. Further investigation into how *S. aureus* interacts with CD47 to facilitate its invasion process remains a valuable and ongoing area of research.

I conducted a comprehensive evaluation of innate immunity and continuously monitored viral loads in the lungs of IAV-infected mice up to 10 dpi. My observations revealed that there were no significant differences in viral titers between *CD47^{fl/fl}*, *CD47^{Foxj1}*, and *CD47^{LysM}* mice at 2, 3, 4, and 7 dpi (Figure 15J and 15K), as well as in IFN- λ 2/3 levels (Figure 15G) and viral loads (Figure 15H and 15I) between *CD47^{fl/fl}* mice and *CD47^{Foxj1}* mice at 10 dpi. These findings suggest that, at the time points examined, CD47 deficiency in ciliated cells or myeloid cells does not seem to have a substantial impact on innate immunity.

A previous study has highlighted the crucial role of CD47 as an "eat me" signal critical for macrophage clearance of neutrophils that have ingested *S. aureus*, leading to increased infection in the absence of CD47⁶³. While prior research has focused on CD47's involvement in immune cell communication during bacterial infection, my findings emphasize a distinct aspect where CD47 expressed in epithelial cells during viral infection serves as an attachment site for secondary bacterial infection. Hence, it is conceivable that the roles of CD47 on epithelial cells versus myeloid cells are distinct, necessitating further investigation to fully understand these differences.

V. CONCLUSION

In summary, I have established that influenza virus triggers the expression of CD47 on the surface of ciliated cells in an NF- κ B-dependent manner, creating an environment that promotes the attachment and proliferation of opportunistic pathogens. Furthermore, my research has shown that inhibiting the induction of airway epithelial CD47 during viral infection can mitigate the detrimental consequences of subsequent bacterial infection. These findings offer fresh perspectives on the susceptibility of virus-infected individuals to bacterial co-infections and propose CD47 as an innovative and promising therapeutic target for super-infection.

REFERENCES

1. Morens DM, Taubenberger JK, Fauci AS. Predominant role of bacterial pneumonia as a cause of death in pandemic influenza: Implications for pandemic influenza preparedness. *J Infect Dis.* 2008;198:962–970
2. Estenssoro E, Ríos FG, Apezteguía C, Reina R, Neira J, Ceraso DH, et al. Pandemic 2009 influenza A in Argentina: a study of 337 patients on mechanical ventilation. *Am. J. Respir. Crit. Care Med.* 2010;182(1):41-48.
3. Rice TW, Rubinson L, Uyeki TM, Vaughn FL, John BB, Miller RR 3rd, et al. Critical illness from 2009 pandemic influenza A virus and bacterial coinfection in the United States. *Crit. Care Med.* 2012;40(5):1487-1498.
4. McCullers JA. The co-pathogenesis of influenza viruses with bacteria in the lung. *Nat. Rev. Microbiol.* 2014;12(4):252–262.
5. Georas SN, Rezaee F. Epithelial barrier function: at the front line of asthma immunology and allergic airway inflammation. *J. Allergy Clin. Immunol.* 2014;134(3):509-520.
6. Rezaee F, Georas SN. Breaking barriers. New insights into airway epithelial barrier function in health and disease. *Am. J. Respir. Cell Mol. Biol.* 2014;50(5):857-869.
7. Sajjan U, Wang Q, Zhao Y, Gruenert DC, Hershenson MB. Rhinovirus Disrupts the Barrier Function of Polarized Airway Epithelial Cells. *Am. J. Respir. Crit. Care Med.* 2008;178:1271–1281.
8. Comstock AT, Ganesan S, Chattoraj A, Faris AN, Margolis BL, Hershenson MB, et al. Rhinovirus-induced barrier dysfunction in polarized airway epithelial cells is mediated by NADPH oxidase 1. *J. Virol.* 2011;85(13):6795-6808.
9. Rezaee F, DeSando SA, Ivanov AI, Chapman TJ, Knowlden SA, Beck LA, et al. Sustained protein kinase D activation mediates respiratory syncytial virus-induced airway barrier disruption. *J. Virol.* 2013 Oct;87(20):11088-11095.
10. Yeo NK, Jang YJ. Rhinovirus infection-induced alteration of tight junction and adherens junction components in human nasal epithelial cells. *Laryngoscope.*

- 2010;120(2):346-352.
11. Navarini AA, Recher M, Lang KS, Georgiev P, Meury S, Bergthaler A, et al. Increased susceptibility to bacterial superinfection as a consequence of innate antiviral responses. *Proc. Natl Acad. Sci. USA.* 2006;103(42):15535-15539.
 12. Sun K, Metzger DW. Inhibition of pulmonary antibacterial defense by interferon-gamma during recovery from influenza infection. *Nat. Med.* 2008;14(5):558-564.
 13. Kudva A, Scheller EV, Robinson KM, Crowe CR, Choi SM, Slight SR, et al. Influenza A inhibits Th17-mediated host defense against bacterial pneumonia in mice. *J. Immunol.* 2011;186:1666-1674.
 14. Nakamura S, Davis KM, Weiser JN. Synergistic stimulation of type I interferons during influenza virus coinfection promotes *Streptococcus pneumoniae* colonization in mice. *J. Clin. Invest.* 2011;121(9):3657-3665.
 15. Lee B, Robinson KM, McHugh KJ, Scheller EV, Mandalapu S, Chen C, et al. Influenza-induced type I interferon enhances susceptibility to gram-negative and gram-positive bacterial pneumonia in mice. *Am. J. Physiol. Lung. Cell Mol. Physiol.* 2015;309(2):L158-L167.
 16. Major J, Crotta S, Llorian M, McCabe TM, Gad HH, Priestnall SL, et al. Type I and III interferons disrupt lung epithelial repair during recovery from viral infection. *Science.* 2020;369(6504):712-717.
 17. Broggi A, Ghosh S, Sposito B, Spreafico R, Balzarini F, Lo Cascio A, et al. Type III interferons disrupt the lung epithelial barrier upon viral recognition. *Science.* 2020;369(6504):706-712.
 18. Ghoneim HE, Thomas PG, McCullers JA. Depletion of alveolar macrophages during influenza infection facilitates bacterial superinfections. *J. Immunol.* 2013;191(3):1250-1259.
 19. Papi A, Johnston SL. Rhinovirus infection induces expression of its own receptor intercellular adhesion molecule 1 (ICAM-1) via increased NF-kappaB-mediated transcription. *J. Biol. Chem.* 1999;274(14):9707-9720.

20. Avadhanula V, Rodriguez CA, Devincenzo JP, Wang Y, Webby RJ, Ulett GC, et al. Respiratory viruses augment the adhesion of bacterial pathogens to respiratory epithelium in a viral species- and cell type-dependent manner. *J. Virol.* 2006;80:1629–1636.
21. Othumpangat S, Noti JD, McMillen CM, Beezhold DH. ICAM-1 regulates the survival of influenza virus in lung epithelial cells during the early stages of infection. *Virology.* 2016;487:85–94.
22. Sugiyama MG, Gamage A, Zyla R, Armstrong SM, Advani S, Advani A, et al. Influenza Virus Infection Induces Platelet-Endothelial Adhesion Which Contributes to Lung Injury. *J Virol.* 2015;90(4):1812-1823.
23. Jang YJ, Wang JH, Kim JS, Kwon HJ, Yeo NK, Lee BJ. Levocetirizine inhibits rhinovirus-induced ICAM-1 and cytokine expression and viral replication in airway epithelial cells. *Antiviral Res.* 2009;81(3):226-233.
24. Wang JH, Kwon HJ, Jang YJ. Rhinovirus enhances various bacterial adhesions to nasal epithelial cells simultaneously. *Laryngoscope.* 2009;119(7):1406-1411.
25. Li N, Ren A, Wang X, Fan X, Zhao Y, Gao GF, et al. Influenza viral neuraminidase primes bacterial coinfection through TGF- β -mediated expression of host cell receptors. *Proc. Natl. Acad. Sci. USA.* 2015;112:238–243.
26. van der Sluijs KF, van Elden LJ, Nijhuis M, Schuurman R, Florquin S, Shimizu T, et al. Involvement of the platelet-activating factor receptor in host defense against *Streptococcus pneumoniae* during postinfluenza pneumonia. *Am. J. Physiol. Lung Cell Mol. Physiol.* 2006;290(1):L194-L199.
27. Cundell DR, Gerard NP, Gerard C, Idanpaan-Heikkila I, Tuomanen EI. *Streptococcus pneumoniae* anchor to activated human cells by the receptor for platelet-activating factor. *Nature.* 1995;377(6548):435-438.
28. McCullers JA, Rehg JE. Lethal synergism between influenza virus and *Streptococcus pneumoniae*: characterization of a mouse model and the role of platelet-activating factor receptor. *J. Infect. Dis.* 2002;186(3):341-350.

29. Barclay AN, Van den Berg TK. The interaction between signal regulatory protein alpha (SIRP α) and CD47: structure, function, and therapeutic target. *Annu. Rev. Immunol.* 2014;32:25–50.
30. Jaiswal S, Jamieson CH, Pang WW, Park CY, Chao MP, Majeti R, et al. CD47 is upregulated on circulating hematopoietic stem cells and leukemia cells to avoid phagocytosis. *Cell.* 2009;138(2):271–285.
31. Cham LB, Torrez Dulgeroff LB, Tal MC, Adomati T, Li F, Bhat H, et al. Immunotherapeutic blockade of CD47 Inhibitory Signaling Enhances Innate and Adaptive Immune Responses to Viral Infection. *Cell Rep.* 2020;31:107494.
32. Soto-Pantoja DR, Shih HB, Maxhimer JB, Cook KL, Ghosh A, Isenberg JS, et al. Thrombospondin-1 and CD47 signaling regulate healing of thermal injury in mice. *Matrix Biol.* 2014;37:25-34.
33. Isenberg JS, Romeo MJ, Abu-Asab M, Tsokos M, Oldenburg A, Pappan L, et al. Increasing survival of ischemic tissue by targeting CD47. *Circ. Res.* 2007;100(5):712-720.
34. Isenberg JS, Romeo MJ, Abu-Asab M, Tsokos M, Oldenburg A, Pappan L, et al. Treatment of liver ischemia-reperfusion injury by limiting thrombospondin-1/CD47 signaling. *Surgery.* 2008;144(5):752-761.
35. Maxhimer JB, Shih HB, Isenberg JS, Miller TW, Roberts DD. Thrombospondin-1/CD47 blockade following ischemia-reperfusion injury is tissue protective. *Plast Reconstr. Surg.* 2009;124(6):1880-1889.
36. Soto-Pantoja DR, Isenberg JS, Roberts DD. Therapeutic Targeting of CD47 to Modulate Tissue Responses to Ischemia and Radiation. *J. Genet. Syndr. Gene Ther.* 2011;2(2):1000105.
37. Rogers NM, Thomson AW, Isenberg JS. Activation of parenchymal CD47 promotes renal ischemia-reperfusion injury. *J. Am. Soc. Nephrol.* 2012;23(9):1538-1550.
38. Reed M, Luissint AC, Azcutia V, Fan S, O’Leary MN, Quiros M, et al. Epithelial

- CD47 is critical for mucosal repair in the murine intestine in vivo. *Nat. Commun.* 2019;10(1):5004.
39. Wang JH, Lee SH, Kwon HJ, Jang YJ. Clarithromycin inhibits rhinovirus-induced bacterial adhesions to nasal epithelial cells. *Laryngoscope.* 2010;120(1):193-199.
 40. Lo J, Lau EY, Ching RH, Cheng BY, Ma MK, Ng IO, et al. Nuclear Factor Kappa B-Mediated CD47 up-Regulation Promotes Sorafenib Resistance and Its Blockade Synergizes the Effect of Sorafenib in Hepatocellular Carcinoma in Mice. *Hepatology.* 2015;62:534–545.
 41. Akamatsu MA, de Castro JT, Takano CY, Ho PL. Off balance: Interferons in COVID-19 lung infections. *EBioMedicine.* 2021;73:103642.
 42. Mercer RR, Russell ML, Roggli VL, Crapo JD. Cell number and distribution in human and rat airways. *Am. J. Respir. Cell Mol. Biol.* 1994;10:613–624.
 43. Cho HJ, Chung YW, Moon S, Seo JH, Kang M, Nam JS, et al. IL-4 drastically decreases deuterosomal and multiciliated cells via alteration in progenitor cell differentiation. *Allergy.* 2023;78(7):1866-1877.
 44. Lopez-Souza N, Favoreto S, Wong H, Ward T, Yagi S, Schnurr D, et al. In vitro susceptibility to rhinovirus infection is greater for bronchial than for nasal airway epithelial cells in human subjects. *J. Allergy Clin. Immunol.* 2009;123(6):1384-1390.e1382.
 45. Ulanova M., Gravelle S., Barnes R. The role of epithelial integrin receptors in recognition of pulmonary pathogens. *J. Innate Immun.* 2009;1(1):4–17.
 46. Weiser JN, Ferreira DM, Paton JC. *Streptococcus pneumoniae*: transmission, colonization and invasion. *Nat. Rev. Microbiol.* 2018;16:355–367.
 47. Greene C, McDevitt D, Francois P, Vaudaux PE, Lew DP, Foster TJ. Adhesion properties of mutants of *Staphylococcus aureus* defective in fibronectin-binding proteins and studies on the expression of *fnb* genes. *Mol. Microbiol.* 1995;17(6):1143-1152.
 48. Zhang Y, Huang G, Shornick LP, Roswit WT, Shipley JM, Brody SL, et al. A

- transgenic FOXJ1-Cre system for gene inactivation in ciliated epithelial cells. *Am. J. Respir. Cell Mol. Biol.* 2007;36(5):515-519.
49. Groud JA, Dresden BP, Riesmeyer AM, Cooper VS, Bomberger JM, Richardson AR, et al. Novel Requirement for Staphylococcal Cell Wall-Anchored Protein SasD in Pulmonary Infection. *Microbiol. Spectr.* 2022;10(5):e0164522.
 50. Kimaro Mlacha SZ, Peret TC, Kumar N, Romero-Steiner S, Dunning Hotopp JC, Ishmael N, et al. Transcriptional adaptation of pneumococci and human pharyngeal cells in the presence of a virus infection. *BMC Genomics.* 2013;14:378.
 51. Tal MC, Torrez Dulgeroff LB, Myers L, Cham LB, Mayer-Barber KD, Bohrer AC, et al. Upregulation of CD47 is a host checkpoint response to pathogen recognition. *mBio.* 2020;11:e01293–20.
 52. McLaughlin KM, Bojkova D, Kandler JD, Bechtel M, Reus P, Le T, et al. A potential role of the CD47/SIRPalpha axis in COVID-19 pathogenesis. *Curr. Issues Mol. Biol.* 2021;43:1212–1225.
 53. Bojkova D, Klann K, Koch B, Widera M, Krause D, Ciesek S, et al. Proteomics of SARS-CoV-2-infected host cells reveals therapy targets. *Nature.* 2020;583(7816):469-472.
 54. Blanco-Melo D, Nilsson-Payant BE, Liu WC, Uhl S, Hoagland D, Møller R, et al. Imbalanced Host Response to SARS-CoV-2 Drives Development of COVID-19. *Cell.* 2020;181(5):1036-1045.e1039.
 55. de Graaf M, Fouchier RA. Role of receptor binding specificity in influenza A Virus transmission and pathogenesis. *EMBO J.* 2014;33:823–841.
 56. Robinot R, Hubert M, de Melo GD, Lazarini F, Bruel T, Smith N, et al. SARS-CoV-2 infection induces the dedifferentiation of multiciliated cells and impairs mucociliary clearance. *Nat. Commun.* 2021;12(1):4354.
 57. McNab F, Mayer-Barber K, Sher A, Wack A, O’Garra A. Type I interferons in infectious disease. *Nat. Rev. Immunol.* 2015;15:87–103.
 58. Dziwanowska K, Carson AR, Patti JM, Deobald CF, Bayles KW, Bohach GA.

- Staphylococcal fibronectin binding protein interacts with heat shock protein 60 and integrins: role in internalization by epithelial cells. *Infect. Immun.* 2000;68(11):6321-6328.
59. Ghebrehewet S, MacPherson P, Ho A. Influenza. *BMJ.* 2016;355:i6258.
60. Peteranderl C, Herold S, Schmoltdt C. Human Influenza Virus Infections. *Semin. Respir. Crit Care Med.* 2016;37(4):487-500.
61. Bai X, Yang W, Luan X, Li H, Li H, Tian D, et al. Induction of cyclophilin A by influenza A virus infection facilitates group A Streptococcus coinfection. *Cell Rep.* 2021;35(7):109159.
62. Langouët-Astrié C, Oshima K, McMurtry SA, Yang Y, Kwiecinski JM, LaRivière WB, et al. The influenza-injured lung microenvironment promotes MRSA virulence, contributing to severe secondary bacterial pneumonia. *Cell Rep.* 2022;41(9):111721.
63. Greenlee-Wacker MC, Rigby KM, Kobayashi SD, Porter AR, DeLeo FR, Nauseef WM. Phagocytosis of Staphylococcus aureus by human neutrophils prevents macrophage efferocytosis and induces programmed necrosis. *J. Immunol.* 2014;192(10):4709-4717.
64. Chung YW, Cha J, Han S, Chen Y, Gucek M, Cho HJ, et al. Apolipoprotein E and Periostin Are Potential Biomarkers of Nasal Mucosal Inflammation. A Parallel Approach of In Vitro and In Vivo Secretomes. *Am. J. Respir. Cell Mol. Biol.* 2020;62(1):23-34.
65. Kim JI, Lee S, Lee GY, Park S, Bae JY, Heo J, et al. Novel Small Molecule Targeting the Hemagglutinin Stalk of Influenza Viruses. *J. Virol.* 2019;93(17):e00878-19.
66. Askarian F, Uchiyama S, Valderrama JA, Ajayi C, Sollid JUE, van Sorge NM, et al. Serine-Aspartate Repeat Protein D Increases Staphylococcus aureus Virulence and Survival in Blood. *Infect. Immun.* 2016;85(1):e00559-16.
67. Fey PD, Endres JL, Yajjala VK, Widhelm TJ, Boissy RJ, Bose JL, et al. A genetic

- resource for rapid and comprehensive phenotype screening of nonessential *Staphylococcus aureus* genes. *mBio*. 2013;4(1):e00537-12.
68. Chung YW, Lagranha C, Chen Y, Sun J, Tong G, Hockman SC, et al. Targeted disruption of PDE3B, but not PDE3A, protects murine heart from ischemia/reperfusion injury. *Proc. Natl Acad. Sci. USA*. 2015;112(17):E2253-62.
69. Park DY, Kim S, Kim CH, Yoon JH, Kim HJ. Alternative Method for Primary Nasal Epithelial Cell Culture Using Intranasal Brushing and Feasibility for the Study of Epithelial Functions in Allergic Rhinitis. *Allergy Asthma Immunol. Res*. 2016;8(1):69-78.
70. Rajavelu P, Chen G, Xu Y, Kitzmiller JA, Korfhagen TR, Whitsett JA. Airway epithelial SPDEF integrates goblet cell differentiation and pulmonary Th2 inflammation. *J. Clin. Invest*. 2015;125(5):2021-2031.
71. Schliehe C, Flynn EK, Vilagos B, Richson U, Swaminathan S, Bosnjak B, et al. The methyltransferase Setdb2 mediates virus-induced susceptibility to bacterial superinfection. *Nat Immunol* . 2015;16(1):67-74.

ABSTRACT (in Korean)

인플루엔자 바이러스에 의해 유도되는 병원성세균을 통한 세균 중복 감염 유발 시 호흡기 상피세포의 CD47 역할 규명에 대한 연구

< 지도교수 유 지 환 >

연세대학교 대학원 의과학과

문 성 민

호흡기 바이러스 감염은 세균 중복 감염에 대한 숙주의 감수성을 증가시킨다. 그러나, 기도 상피에서의 바이러스 감염과 순차적 세균 감염 사이의 관계는 불분명하다. 본 연구는 인플루엔자 바이러스 감염 후 추가적인 세균 중복 감염 시 기도 상피에서의 CD47의 중요한 역할을 정의한다. 인플루엔자 바이러스 감염 시 유도되는 CD47은 상기도 및 하기도 상피세포의 섬모 세포에서 노출된다는 것을 확인했다. 이러한 CD47 노출은 황색 포도상구균의 부착 부위를 제공하여 상피 세포의 장벽을 파괴한다. 세균 부착 분석 및 체외 풀다운 분석을 통해 황색 포도상구균의 피브로넥틴 결합 단백질(FnBP)이 CD47에 결합하는 구성 요소로 밝혀졌다. 더욱이, 섬모 세포 특이적 CD47 결핍 또는 중화 항체 매개 CD47 불활성화가 생체 내 생존율을 향상시킨다는 것을 발견했다. 결론적으로, 이러한 결과들은 기도 상피세포의 CD47과 병원성 세균 FnBP 사이의 상호작용의 파괴가 세균 중복 감염의 해로운 영향을 개선할 수 있음을 시사한다.

핵심되는 말: 인플루엔자 바이러스, 황색 포도상구균, CD47, 기도상피, 세균 중복 감염, 밀착연접; ZO-1, 피브로넥틴 결합 단백질; FnBP